

# First-principles determination of refractory binary alloy mechanical properties for the microscopic design of complex structural materials

Surya T. Bijjala<sup>a</sup>, Susan R. Atlas<sup>b</sup>, Pankaj Kumar<sup>c,\*</sup>

<sup>a</sup>Department of Mechanical Engineering, University of New Mexico, 87131, Albuquerque, USA

<sup>b</sup>Department of Chemistry and Chemical Biology, Department of Physics and Astronomy, and Center for Quantum Information and Control, University of New Mexico, 87131, Albuquerque, USA

<sup>c</sup>Department of Mechanical Engineering, University of New Mexico, 87131, Albuquerque, USA

## Abstract

The elastic tensor provides valuable insight into the mechanical behavior of a material with lattice strain, such as disordered binary alloys. Density functional theory (DFT)-based methods provide a powerful mechanism for computing and probing the microscopic features of elastic tensor-related properties. Here we present results for the rigid-ion and relaxed-ion elastic tensors computed using density functional perturbation theory (DFPT), for a comprehensive set of structural refractory body-centered cubic (BCC) binary alloys of molybdenum (Mo), niobium (Nb), tantalum (Ta), and tungsten (W). Intermediate quantities (force-response internal-strain tensor,  $\Lambda$ , and displacement-response internal-strain tensor,  $\Gamma$ ) needed to compute the relaxed-ion elastic tensor are used here to map heterogeneity in elastic constants at each lattice site in a given alloy and associated relaxation fields. Derived polycrystalline aggregate properties—the bulk modulus ( $B$ ), shear modulus ( $G$ ), Young’s modulus ( $E$ ), and Poisson’s ratio ( $\nu$ ) and elastic anisotropy—are reported as a function of composition for all binaries. Pugh’s ratio ( $B/G$ ) and the Cauchy pressure ( $C'$ ) derived from computed elastic moduli are analyzed in order to evaluate the effect of alloying on the mechanical properties of the refractory BCC binary alloys. The computed mechanical properties data for the parent unary materials and binary alloys at systematically-varied Mo, Nb, Ta, and W compositions are in excellent agreement with available experimental data. These results, together with computed microscopic field data, establish a foundation for the principled design of compositionally-complex, high-temperature-structural refractory alloys with desired elastic properties.

**Keywords:** Refractory alloy, Density functional theory, Compositionally-complex alloys, Elastic properties, Property anisotropy

## 1. Introduction

The elastic tensor [1] and its elastic constant components give a complete description, in terms of deformation, of material response under external stress within the elastic limit. Inducing lattice strain through alloying is a key design strategy for tuning and optimizing the properties of compositionally-complex materials [2, 3] such as multi-component refractory alloys comprised of four or more principal elements and alloying elements [4]. The elastic tensor can therefore serve as a valuable quantitative probe of elastic strain effects associated with changes in chemical composition, and their

impact on mechanical [5, 6, 7, 8, 9], electronic [10, 11], thermodynamic [12, 13], and structural [14, 15, 16] properties in these materials. A particular challenge for refractory alloy design based on Mo, W, Nb, and Ta—materials that have excited considerable interest [17, 18] as next-generation high-temperature structural materials [19] and are the focus of the present work—lies in achieving an optimal balance among technologically-desirable properties such as ductility and yield strength.

Elastic tensor-derived quantities such as Pugh’s ratio of bulk to shear modulus ( $B/G$ ) [20], the Cauchy pressure ( $C_{12} - C_{44}$ ) [21], and Poisson’s ratio (negative ratio of transverse to axial strain) [22] have long been used as metrics for predicting trends in ductility in multi-principal-element refractory alloys [23, 24]. For materials with cubic crystal structures, an empiri-

\*Corresponding author

Email address: pankaj@unm.edu (Pankaj Kumar)

cal correlation observed between the Young’s modulus-normalized Cauchy pressure  $(C_{12} - C_{44})/E$  and Pugh’s ratio criteria for the ductile-to-brittle transition [25] was subsequently shown to be exact [26]. Recent studies on empirical solid solution strengthening models have shown that shear modulus mismatch has a strong effect on the yield strength of BCC alloys [27, 28]: these models are used as a guide in the search for high strength, ductile BCC refractory high entropy alloys (RHEAs) for high-temperature applications [29, 30]. At the microscopic level, elastic constants have been used in the parameterization of traditional [31] and machine-learned [32] interatomic potentials for performing classical molecular dynamics simulations of mesoscale materials properties. Notably, Pettifor’s Cauchy pressure criterion was based on a quantum mechanical bond-order model of the underlying interatomic potential [21], and a microscopic model of the Cauchy pressure has been proposed based on local bonding topologies, with spring constants computed as a function of quantum mechanically-derived atomic effective charges [33].

Refractory alloys show great potential to meet the demands for high temperature materials due to their high melting points and ability to maintain mechanical properties at temperatures higher than current Ni-based superalloys [18]. The refractory elements Nb, Ta, Mo, and W of groups V and VI comprise the BCC structural refractory metals family, characterized by high mechanical strength and melting temperatures [34]. Their structural refractory binary alloys MoNb, MoTa, MoW, NbTa, WNb and WTa form solid solutions of BCC crystal structure across their entire compositional space [35]. For multiple-principal-element alloys made of these elements, only BCC crystal structures are observed experimentally, even in cases where multiple phases are present, and independent of manufacturing technique [4]. However, experimental development and property optimization of novel refractory alloys present numerous challenges associated with processing, due to differences in melting temperatures among constituent elements (causing elemental segregation during casting), and the introduction of unwanted oxygen and carbon impurities [36]. Experimental measurements of elastic constants require large single crystals, which can be challenging to fabricate [37]. Moreover, elastic constant measurements are typically reported only for a limited number of alloy classes and compositions, and experiments often exhibit substantial disagreement even between values measured using the same technique and on the same material [38, 39]. Multiple factors can influence differences in reported experimental values, such as impurities and measurement tem-

perature [40].

In light of these experimental challenges, and the combinatorically-large compositional design space that must be explored and optimized in order to discover multi-principal-element refractory alloys with targeted mechanical properties, researchers have increasingly turned to computational approaches [41, 42, 43, 44]. Here we establish a first-principles modeling framework based on density-functional theory (DFT) [45, 46] for performing computationally-efficient studies of elastic tensor properties of disordered alloys, validated for systematically-varied Mo, Nb, Ta, and W binary alloy compositions. This framework is intended to serve as the starting point for the principled design of more complex BCC structural refractory alloys with desired mechanical properties, using computed microscopic field (present work), and bandstructure data [35], in the much larger compositional space of 4+ principal elements. DFT, as implemented in state-of-the-art planewave pseudopotential periodic electronic structure codes such as Abinit [47], provides direct access to the computation of energies and stresses for obtaining the elastic tensors of the materials, with only atomic structure and nuclear charges as inputs. The availability of large, high-quality databases of DFT energies and crystal structures such as those of the Materials Project [48] and AFLOW [49], enables validation, and assessment of the effects of different levels of theory for ordered unary and binary materials, in advance of extending calculations to disordered alloys with larger numbers of elements.

The principal quantity to be considered is the elastic tensor and its elastic constant components. In the traditional approach, the elastic constants  $C_{ij}$  are obtained by computing either the total energy or the stress of a crystal at different strains [40, 50, 51, 52, 53]. The stress-strain relation is given by:

$$\begin{bmatrix} \sigma_{11} \\ \sigma_{22} \\ \sigma_{33} \\ \sigma_{23} \\ \sigma_{13} \\ \sigma_{12} \end{bmatrix} = \begin{bmatrix} C_{11} & C_{12} & C_{13} & C_{14} & C_{15} & C_{16} \\ C_{12} & C_{22} & C_{23} & C_{24} & C_{25} & C_{26} \\ C_{13} & C_{23} & C_{33} & C_{34} & C_{35} & C_{36} \\ C_{14} & C_{24} & C_{34} & C_{44} & C_{45} & C_{46} \\ C_{15} & C_{25} & C_{35} & C_{45} & C_{55} & C_{56} \\ C_{16} & C_{26} & C_{36} & C_{46} & C_{56} & C_{66} \end{bmatrix} \begin{bmatrix} s_{11} \\ s_{22} \\ s_{33} \\ 2s_{23} \\ 2s_{13} \\ 2s_{12} \end{bmatrix} \quad (1)$$

where  $\sigma$  is the  $6 \times 1$  stress tensor, the  $C_{ij}$  are the elastic constants, and  $s$  is the  $6 \times 1$  strain tensor in Voigt notation [54]. To obtain all 21 independent elastic constants, stress tensors must be computed from fully-relaxed DFT calculations for each applied strain  $s_{ij}$  (total of 6 independent strain components) for 4 different strain magnitudes [55]. Including the initial geome-

try optimization of the structure, a total of 24+1 independent calculations are required to compute the elastic tensor [40, 56, 57]. For each structure with its applied strain, the atomic positions must be re-relaxed prior to the computation of the stresses. These methods are therefore computationally expensive, especially for low-symmetry structures. Such low-symmetry systems are found in solid solution alloys where atomic mismatch and random configurations break the symmetry of the parent structures, as demonstrated in BCC refractory binary alloys [35]. For this reason, BCC disordered alloys are often approximated as high-symmetry structures with only three independent elastic constants ( $C_{11}$ ,  $C_{12}$  and  $C_{44}$ ), in order to reduce the number of computations required to compute the elastic tensor [5, 58, 59, 60, 61]. In addition, since the stress-strain approach requires the selection of specific strain magnitudes in order to obtain the full elastic tensor, it is necessary to vary the strain magnitudes and confirm that the chosen applied strains are within the elastic limit.

A faster and simpler alternative, appropriate for scaling to multi-principal-element alloys, is by analytical differentiation of the energy using linear response theory [62, 63, 64, 65]. In this method, the elastic tensor is obtained by expanding the total energy with respect to infinitesimal perturbation of the system using density functional perturbation theory (DFPT) [66]. DFPT was initially developed for norm-conserving pseudopotentials (NCPPs) [67] and later extended to the projector augmented-wave (PAW) method by Martin *et al.* [68]. DFPT implemented with NCPPs has been shown to be successful in the computation of the elastic tensor for a variety of materials [69, 70, 71], and the drawbacks of the stress-strain method for previously unexplored complex materials—the need for different preset strains as a function of material and composition, and the potential generation of unphysical structures—are avoided.

Within the DFPT framework, the elastic tensor can be evaluated as the *rigid-ion* elastic tensor,  $C_{ij}^{rigid}$ , or as the *relaxed-ion* elastic tensor  $C_{ij}^{relaxed}$  [62, 63, 64, 65].  $C_{ij}^{rigid}$  is computed with the relaxed initial structure, and strain as the perturbation;  $C_{ij}^{relaxed}$  is a correction to the rigid-ion elastic tensor, with both strain and atomic displacements (nuclear relaxations) as the perturbations. In contrast to the traditional stress-strain method, each of these elastic tensor calculations requires only a single DFPT calculation, and both  $C_{ij}^{rigid}$  and  $C_{ij}^{relaxed}$  provide essential information about the elastic response of a material. The relaxed-ion elastic tensor is the quantity that will correspond most closely to experiment.

Comparison of the rigid-ion and relaxed-ion results

allows an assessment of the accuracy of the rigid-ion approximation, as well as enabling the mapping of the relaxation field of a disordered alloy. These maps can provide quantitative measures of the microscopic elastic response of the binary alloys, for later input to models of more complex multi-principal-element alloys. We define the nuclear relaxation elastic tensor  $C_{ij}^{nuclear}$  as the difference between the corresponding rigid-ion and relaxed-ion quantities [65]:

$$C_{ij}^{relaxed} = C_{ij}^{rigid} - C_{ij}^{nuclear} \quad (2)$$

where

$$C_{ij}^{rigid} = \frac{d\sigma_i}{ds_j} = \frac{\partial^2 E}{\partial s_i \partial s_j}. \quad (3)$$

$E$  is the energy per undeformed unit cell volume, and the  $s_i$  are lattice deformations.

Non-zero nuclear-relaxation contributions in binary alloys are due to lattice distortions induced by the alloying elements, leading to forces between atoms in a finite strain state. Nuclear-relaxation contributions have previously been used to understand the effect of stress on piezoelectric coefficients and elastic constants by decomposing them into a purely electronic rigid-ion contribution and nuclear-relaxation contribution resulting from the atomic rearrangements in the strained state [72, 73]. In a study by Zhang *et al.* [74], the nuclear-relaxation term was decomposed into lattice point-specific relaxation contributions in order to elucidate the microscopic origin of the piezoelectric effect in  $\alpha$ -quartz. The construction of relaxed-ion elastic constants implemented here is accomplished in analogous fashion [65]. While the rigid-ion contribution to an elastic constant is uniform across the lattice, nuclear-relaxation contributions vary as a function of lattice site, as the type of atom varies at each lattice site in the disordered binary alloys. Hence decomposition of nuclear contributions enables the evaluation of the relaxation field in a disordered binary alloy. Hereafter, the terms “nuclear-relaxation contributions” and “relaxation values” will be used interchangeably.

In the present work, we utilize DFT+DFPT to compute the single-crystal, relaxed-structure elastic tensors of the six BCC refractory binary alloys of (Mo, Nb, Ta, W)—MoNb, MoTa, MoW, NbTa, MoTa, and MoW—as a function of composition. The disordered alloys are modeled as supercells constructed using the special quasi-random structures (SQS) method [75]. The relaxed disordered structures are then used to compute the rigid-ion and relaxed-ion elastic tensors based on DFPT. We assess the effectiveness of DFPT in providing accurate elastic tensors through detailed comparison of

elastic constants with available experimental data. The composition-dependent calculations serve as an important test of the ability of the SQS method to accurately model disorder in these alloys. Mechanical properties  $B$ ,  $G$ , and  $E$ , and the elastic anisotropy and ductility metrics  $B/G$  and  $C'$  derived from the computed elastic moduli are reported as a function of composition for all binaries. Computed relaxation fields for the Voigt-averaged elastic constants and shear modulus are presented for all binaries and discussed in terms of constituent element chemistry. In addition, we discuss the computational efficiency of DFPT compared to traditional stress-strain methods. The in-depth understanding of trends in elastic properties and anisotropy in the disordered refractory binary alloys gained in this work through the decomposition of elastic constants into electronic and nuclear contributions is expected to contribute to new microscopic alloy computational strategies for designing refractory alloys for high-temperature applications.

## 2. Computational Methods

We used the open-source, periodic plane wave pseudopotential electronic structure code Abinit [76, 47] for all DFT calculations, employing the Perdew, Burke, and Ernzerhof (PBE) generalized gradient approximation (GGA) exchange-correlation functional [77], with corresponding PBE norm-conserving pseudopotentials [78]. We note that while meta-GGA methods such as rSCAN [79] and parameterized DFT+ $U$  [80] approaches have seen growing popularity for computing the properties of ordered systems with 1-3 elements [81], the corresponding pseudopotentials are not currently available, and the accuracy of these functionals for complex disordered systems with 5+ elements has yet to be assessed. Since the present work is intended as a starting point for scaling up to larger refractory alloy systems with increased chemical complexity, the PBE functional is utilized throughout this work, to ensure a uniform level of theory across all alloys.

The plane waves for each system were expanded up to a kinetic energy of 30 Ha, with each structure converged until the total residual differences in the potential were  $< 10^{-12}$  Ha, corresponding to convergence to  $10^{-6}$  bohr for lattice constants, and atomic forces converged to  $< |\pm 0.01|$  mHa/bohr. Following careful convergence studies, we adopted a  $\Gamma$ -centered Monkhorst–Pack [82] special  $k$ -point grid with a density of 50  $k$ -points per  $\text{\AA}$  for all systems.

Initial benchmark studies were performed on bulk Mo, Nb, Ta, W in order to determine appropriate com-

putational parameters for the binary alloy calculations. We computed the lattice constants, bulk moduli, cohesive energies, elastic constants, and (100), (110), (111) surface energies for elemental Mo, W, Nb, and Ta, and compared our results with available experimental data, using three different pseudopotentials: the FHI norm-conserving pseudopotentials ( $d$  valence electrons only) tabulated at the Abinit website [83], pseudo-dojo [78] NCPPs ( $s$ ,  $p$  and  $d$  valence electrons) available at [84], and projector augmented-wave (PAW) pseudopotentials [85] ( $s$ ,  $p$  and  $d$  valence electrons), tabulated at the Abinit website [83]. Computed properties using the FHI NCPPs showed an average deviation of  $\approx 1\%$  compared to available experiments, across all computed properties for Mo, Nb and Ta, but an average deviation of  $\approx 9\%$  for W. For the pseudo-dojo NCPPs and PAW-based pseudopotentials, computed properties agreed well with experiment, with an average deviation of  $\approx 1.5\%$  for all elements and across all properties. Detailed results are reported in [35]. Given the comparable performance of the pseudo-dojo NCPP and PAW pseudopotentials, and since DFPT is not yet implemented for PAW-based pseudopotentials in Abinit, the pseudo-dojo NCPPs were used throughout this work.

### 2.1. Construction of disordered binary alloy supercells and structure optimization

The special quasi-random structure (SQS) method was used to construct optimally-disordered supercells for modeling the six binaries. The SQS supercells were constructed using the MCSQS [75] module of the open source ATAT [86] software package. Structures with up to four-way correlations were considered, consistent with a range of  $3\times$  the lattice constant ( $\sim 9$ - $10$   $\text{\AA}$  for the binaries considered here). This range was determined based on our previous surface energy benchmarking studies for the bulk elements [35], which showed that atomic interactions were not significant beyond  $\approx 10$   $\text{\AA}$ . For all binaries and compositions, this procedure yielded 16-atom supercells with conventional BCC unit cells stacked in a  $2 \times 2 \times 2$  fashion. Our construction is consistent with the previous work of Jiang *et al.* [87] on BCC MoNb, WTa, and CrFe, who performed extensive convergence studies of SQS supercell sizes for these binaries, and similarly concluded that 16-atom SQS's are the optimal choice in terms of computational efficiency and accuracy of results. The input SQS binary structures were constructed using lattice parameters obtained from the rule of mixtures applied to the constituent element lattice constants. Analogous to the procedure used for the bulk elements, the cell geometry (cell shape and volume) of each binary was optimized to converge the

potential to  $< 10^{-12}$  Ha. For the binaries, 50  $k$ -points per Å yielded  $8 \times 8 \times 8$  special  $k$ -point grids. The Fermi surface of each system was integrated using Gaussian smearing [88] with a width of 0.005 Ha. 10 valence bands/atom were used.

## 2.2. Density functional perturbation theory

Converged atomic structures obtained from geometry optimization calculations were used as input to the DFPT elastic tensor evaluations.  $10 \times 10 \times 10$   $k$ -point grids were used in the DFPT calculations. This ensured a clear separation between occupied and empty orbitals, allowing the application of DFPT to these binary metal alloys [66]. Abinit uses crystal symmetry to optimize computational efficiency. Since the structural relaxation of SQS supercells results in a loss of symmetry during unconstrained DFT relaxations, the Abinit symmetry checker was turned off in all calculations. DFPT calculations were carried out on relaxed structures in order to obtain derivatives of the occupied wave functions with respect to homogeneous strain perturbations  $s_i$  (uniaxial and shear strains). The computed energy derivatives were used to compute the rigid-ion elastic tensors using the Analysis of Derivative DataBase (anaddb) [67, 89] module of Abinit.

Computation of the relaxed-ion elastic tensor requires determination of two intermediate quantities: the force-response internal strain tensor  $\Lambda_{mj}$  and the displacement-response internal strain tensor  $\Gamma_{mn}$ , both associated with periodicity-preserving atomic displacements  $u_m$ . These are computed as [65]:

$$C_{ij}^{\text{relaxed}} = C_{ij}^{\text{rigid}} - C_{ij}^{\text{nuclear}} \quad (4)$$

$$C_{jk}^{\text{nuclear}} = \frac{\Gamma_{nj}\Lambda_{nk}}{\Omega_0} \quad (5)$$

where

$$\Lambda_{nk} = -\Omega_0 \frac{\partial^2 E}{\partial u_n \partial s_k} \quad (6)$$

$$\Gamma_{nj} = \Lambda_{mj} (K^{-1})_{mn} \quad (7)$$

$$K_{mn} = \Omega_0 \frac{\partial^2 E}{\partial u_m \partial u_n}, \quad (8)$$

$E$  is the energy per undeformed unit cell volume, and  $\Omega_0$  is the initial volume of the crystal.

## 2.3. Elastic properties

Within continuum elasticity theory, the elastic tensor of cubic structures [90], including BCC crystals, have three independent elastic constants:  $C_{11}$ ,  $C_{12}$ , and  $C_{44}$ . Since, as previously noted, full relaxation of the SQS

structures breaks cubic symmetry, to enable comparison of DFPT results with experiment, the average elastic constants in the cubic structures were calculated using a method similar to that employed in the Voigt-Hill approach [9]:

$$\begin{aligned} \bar{C}_{11} &= \frac{c_{11} + c_{22} + c_{33}}{3} \\ \bar{C}_{12} &= \frac{c_{12} + c_{23} + c_{31}}{3} \\ \bar{C}_{44} &= \frac{c_{44} + c_{55} + c_{66}}{3} \end{aligned} \quad (9)$$

To obtain composition-dependent values of these Voigt-averaged elastic constants, thermodynamic curve fitting was performed using a Redlich-Kister [91] polynomial. Originally developed for fitting Gibbs free energies as a function of composition, it has also been used to fit elastic properties as a function of composition [6, 92, 93]:

$$\begin{aligned} \bar{C}_{ij}^{AB}(x_A) &= x_A \bar{C}_{ij}^A + (1 - x_A) \bar{C}_{ij}^B \\ &+ x_A(1 - x_A)(I_0 + I_1(2x_A - 1)), \end{aligned} \quad (10)$$

where  $x_A$  is the atomic fraction of element A, and  $\bar{C}_{ij}^{AB}(x_A)$  is the elastic constant of the AB binary with fractional composition  $x_A$  of A.  $\bar{C}_{ij}^A$  and  $\bar{C}_{ij}^B$  are the elastic constants of pure A and B respectively, and  $I_0$  and  $I_1$  are interaction fitting parameters. Eq. (10) will be used to fit the elastic constant curves reported in Section 3 below.

Based on the computed average elastic constants, the polycrystalline aggregate elastic moduli  $B$  (bulk modulus),  $G$  (shear modulus), and  $E$  (Young's modulus) and Poisson's ratio  $\nu$  were obtained using the Voigt approximation [54], which assumes a uniform strain in the crystal and gives an upper bound that correlates with the maximum value of a given property:

$$B_{\text{Voigt}} = \frac{\bar{C}_{11} + 2\bar{C}_{12}}{3} \quad (11)$$

$$G_{\text{Voigt}} = \frac{\bar{C}_{11} - \bar{C}_{12} + 3\bar{C}_{44}}{3} \quad (12)$$

$$E_{\text{Voigt}} = \frac{9B_{\text{Voigt}}G_{\text{Voigt}}}{3B_{\text{Voigt}} + G_{\text{Voigt}}} \quad (13)$$

The degree of elastic anisotropy for all binary alloys is characterized here using the shear  $A_G$  and Young's  $A_E$  anisotropy metrics [94, 95]:

$$A_G = \frac{S_{44} + S_{66}}{2S_{44}} \quad (14)$$

$$A_E = \frac{S_{11}}{S_{33}}, \quad (15)$$

where the  $S_{ij}$  are the elements of compliance tensor, the inverse of the elastic tensor [1].

#### 2.4. Nuclear-relaxation contributions

If we decompose the intermediate quantities  $\Lambda_{nk}$  and  $\Gamma_{nj}$  (Eqs. (6) and (7)) used in computing the relaxed-ion elastic tensor, into nuclear-relaxation contributions from each lattice site  $\alpha$ , Eq. (5) can be rewritten as:

$$C_{jk}^{\text{nuclear}} = \frac{1}{V_0} \sum_{\alpha=1}^N \left( \sum_{i=1, \dots, 6} \Gamma_{\alpha j}^i \Lambda_{\alpha k}^i \right), \quad (16)$$

where  $N$  is number of atoms in the supercell, and the inner summation is over directions in Voigt notation. A similar decomposition of  $G$  into nuclear-relaxation contributions can be accomplished by expressing  $G_{\text{Voigt}}$  in terms of the  $\bar{C}_{ij}$ :

$$\begin{aligned} G_{\text{Voigt}} &= \frac{\bar{C}_{11} - \bar{C}_{12} + 3\bar{C}_{44}}{3} \\ &= \frac{\bar{C}_{11}^{\text{rigid}} - \bar{C}_{11}^{\text{nuclear}} - (\bar{C}_{12}^{\text{rigid}} - \bar{C}_{12}^{\text{nuclear}})}{3} \\ &\quad + \frac{3(\bar{C}_{44}^{\text{rigid}} - \bar{C}_{44}^{\text{nuclear}})}{3} \\ &= \frac{\bar{C}_{11}^{\text{rigid}} + \bar{C}_{12}^{\text{rigid}} + 3\bar{C}_{44}^{\text{rigid}}}{3} \\ &\quad - \frac{\bar{C}_{11}^{\text{nuclear}} + \bar{C}_{12}^{\text{nuclear}} + 3\bar{C}_{44}^{\text{nuclear}}}{3}. \end{aligned} \quad (17)$$

These decompositions of the elastic constants and shear modulus into lattice-dependent nuclear relaxation contributions will be used in the relaxation field analysis of Section 3.5.

### 3. Results

#### 3.1. Rigid-ion vs. relaxed-ion elastic constants

The rigid-ion and relaxed-ion tensors were computed for the binary alloys as described in Section 2. Prior to proceeding with further analysis, we confirmed that the results for both the rigid-ion and relaxed-ion elastic tensors satisfied the well-known Born stability criteria [14]:

$$C_{11} - C_{12} > 0; \quad C_{11} + 2C_{12} > 0; \quad C_{44} > 0 \quad (18)$$

and condition for mechanical stability of solids under zero stress [15, 96]:

$$\begin{aligned} C_{11}^2 - C_{12}^2 > 0, \quad C_{11} > 0 \\ \lambda > 0, \end{aligned} \quad (19)$$

where  $\lambda$  is the vector of six eigenvalues of the  $6 \times 6$  elastic tensor.

The three independent Voigt-averaged elastic constants,  $\bar{C}_{11}$ ,  $\bar{C}_{12}$  and  $\bar{C}_{44}$ , were computed together with their standard deviation values, for each of the BCC binary alloys starting from their rigid-ion and relaxed-ion elastic tensors. The results are listed in Table 1 for three different compositions per AB alloy: A = 25 at.%, 50 at.%, and 75 at.%. The standard deviation  $\sigma_{C_{11}}$  was computed as:

$$\sigma_{C_{11}} = \frac{1}{3} [(\bar{C}_{11} - C_{11})^2 + (\bar{C}_{11} - C_{22})^2 + (\bar{C}_{11} - C_{33})^2]^{1/2}, \quad (20)$$

and the standard deviations for  $\bar{C}_{12}$  and  $\bar{C}_{44}$  were computed similarly. The standard deviation values are observed to be non-zero for both the rigid-ion and relaxed-ion elastic tensors in the binary alloys of A = 25 at.% and 75 at.%, and zero in the binary alloys of A = 50 at.% for all  $\bar{C}_{11}$ ,  $\bar{C}_{12}$  and  $\bar{C}_{44}$ . The standard deviations are of similar magnitudes for both the rigid-ion and relaxed-ion methods, with no particular trend observed among the binary alloys.

The differences between the rigid-ion and relaxed-ion values in Table 1 correspond to nuclear relaxation effects (Eq. (2)). For  $\bar{C}_{11}$ , nuclear relaxation effects for the same-group binary alloys MoW and NbTa are close to 0 at all compositions. However, in the binary alloys MoNb, MoTa, WNb and WTa, whose constituent elements come from different groups (V and VI) of the Periodic Table, nuclear relaxation effects are maximized at A = 50 at.%, with the ordering (WTa  $\approx$  WNb) > (MoTa  $\approx$  MoNb).

For  $\bar{C}_{12}$ , WNb exhibits the greatest nuclear relaxation effect at all compositions, with maximum value at A = 50 at.%. A similar trend to that of  $\bar{C}_{11}$  is observed in the same-group binary alloys. However, in different-group binary alloys, MoTa exhibits negative relaxations at all compositions, with a maximum magnitude of nearly 1 GPa at A = 50 at.% and values close to 0 at A = 25 at.% and 75 at.%. This is notable, since a negative relaxation value corresponds to a greater relaxed-ion elastic constant value compared to the rigid-ion elastic constant value—i.e., it reflects improvement in the elastic constant property with alloying. Unlike for  $\bar{C}_{11}$ , no common trend in  $\bar{C}_{12}$  is observed in different-group binary alloys.

In the case of  $\bar{C}_{44}$ , there is a positive nuclear relaxation effect for all compositions, but no common trend is observed for the same-group binary alloys. The relaxation values for MoW are near zero for all compositions, while the values for NbTa are larger and positive

across all compositions, with a peak value at  $A = 50$  at.%. Among different group binary alloys, WNb shows positive but near-zero values for all compositions, while MoNb, MoTa and WTa, show a finite positive relaxation value. A common trend of peak nuclear relaxation value at  $A = 25$  at.% followed by  $A = 50$  at.% and  $A = 75$  at.% is observed for three of the different-group binary alloys, with magnitude ordering  $\text{MoTa} > \text{WTa} > \text{MoNb}$ .

### 3.2. Rigid-ion elastic constants

Despite the lattice distortions in the binary alloys, the magnitudes of the relaxations lie within the range of the standard deviations and within 2% of the rigid-ion elastic constant values. These are also well within differences in experimental values, which can be as high as 10% [38, 39], depending on the experimental conditions and technique employed. Hence, the computationally faster rigid-ion elastic tensor calculations were performed for the additional compositions of  $A = 12.5$  at.%,  $37.5$  at.%,  $62.5$  at.% and  $87.5$  at.% for all of the AB binary alloys. This allowed us to capture the effects of alloying on the elastic constants of BCC refractory binary alloys for an extended set of compositions.

Fig. 1 compares the calculated rigid-ion elastic constants ( $\bar{C}_{11}^{\text{rigid}}$ ,  $\bar{C}_{12}^{\text{rigid}}$  and  $\bar{C}_{44}^{\text{rigid}}$ ) for all compositions (filled diamonds) with experimental values (stars) for the binary alloys. The rigid-ion elastic constants are fitted to the Redlich-Kister polynomial given in Eq. (10) (solid line). For the same-group binary alloys (Figs. 1(c) and (d)), elastic constants are observed to vary linearly, similar to the empirical rule of Vegard's law [97], while nonlinear behavior is observed for the different-group binary alloys. For the different-group binary alloys, the Ta-containing binary alloys (Figs. 1(b) and (f)) exhibit a greater degree of nonlinearity compared to the Nb-containing binary alloys (Figs. 1(a) and 1(e)). For  $\bar{C}_{11}^{\text{rigid}}$  and  $\bar{C}_{44}^{\text{rigid}}$  in the different-group binary alloys, a negative deviation from Vegard's law is observed for the compositions with  $X > 50$  at.% where X is the element with lower elastic modulus value of the constituent elements. However, for  $\bar{C}_{12}^{\text{rigid}}$ , the trend is reversed, *i.e.*, a positive deviation from Vegard's law is observed for the compositions when  $X > 50$  at.% where X is the element with lower elastic modulus value of the constituent elements.

#### 3.2.1. Comparison with experiment

Experimental values at room temperature for all elastic constants were obtained from the literature as measured using high-frequency ultrasonic methods. For

MoNb [98], NbTa [99] and WNb [100], elastic constants were obtained by measuring sound velocities using the pulse superposition method, and for MoTa elastic constants were obtained by measuring sound velocities using the thin rod resonance technique. High-frequency methods are generally considered to have higher accuracy than static or low frequency methods [101]. Excellent agreement between the computed rigid-ion elastic coefficients and available experimental data is observed, confirming the accuracy of the rigid-ion method for computing the elastic tensors in the present class of binary alloys. It should be noted that our electronic structure calculations are performed at 0 K, while the experimental results are obtained at 298 K; however, refractory metals/alloys are known for the stability of their mechanical properties in this temperature range [98, 99, 100, 102].

### 3.3. Derived mechanical properties

Polycrystalline elastic moduli were derived from the set of computed, Voigt-averaged rigid-ion elastic constants ( $\bar{C}_{11}^{\text{rigid}}$ ,  $\bar{C}_{12}^{\text{rigid}}$  and  $\bar{C}_{44}^{\text{rigid}}$ ) for the binary alloys as a function of composition. The Voigt method [54] was used to calculate the polycrystalline elastic moduli. Fig. 2 summarizes  $B$ ,  $G$  and  $E$  for all binary alloys. Similar to the behavior observed for the elastic constants, same-group binary alloys exhibit a linear trend as a function of composition (Figs. 2(c) and 2(d)) for all elastic moduli. While  $E > B$  for all MoW compositions,  $E < B$  in NbTa across all compositions. Among different-group binary alloys, the bulk modulus is observed to vary linearly with composition, while  $G$  and  $E$  display nonlinear behavior. Similar to  $\bar{C}_{11}^{\text{rigid}}$ ,  $\bar{C}_{12}^{\text{rigid}}$  and  $\bar{C}_{44}^{\text{rigid}}$ , the deviation from linearity for  $G$  and  $E$  is greater in case of the Ta-containing binary alloys (Figs. 2(b) and (f)) than for the Nb-containing binary alloys (Figs. 2(a) and (e)). Fig. 3 shows Pugh's ratio ( $B/G$ ) and the Cauchy pressure ( $(C_{12} - C_{44})/2$ ) for the binary alloys as a function of composition. As noted above, Pugh's ratio  $B/G$  [20] and the Cauchy pressure [21, 103] are widely-used to anticipate the ductility of an alloy. A material is expected to exhibit brittle behavior if Pugh's ratio is less than 2 [104, 25, 105], and is intrinsically ductile if the Cauchy pressure is positive [21, 103]. Similar to the behavior observed for the elastic constants and elastic moduli, MoW and NbTa show a linear trend as a function of composition for both Pugh's ratio and the Cauchy pressure (Figs. 3(c) and 3(d)). Among different-group binary alloys, Nb-containing binary alloys displayed different behavior for Pugh's ratio and the Cauchy pressure as a function of composition,

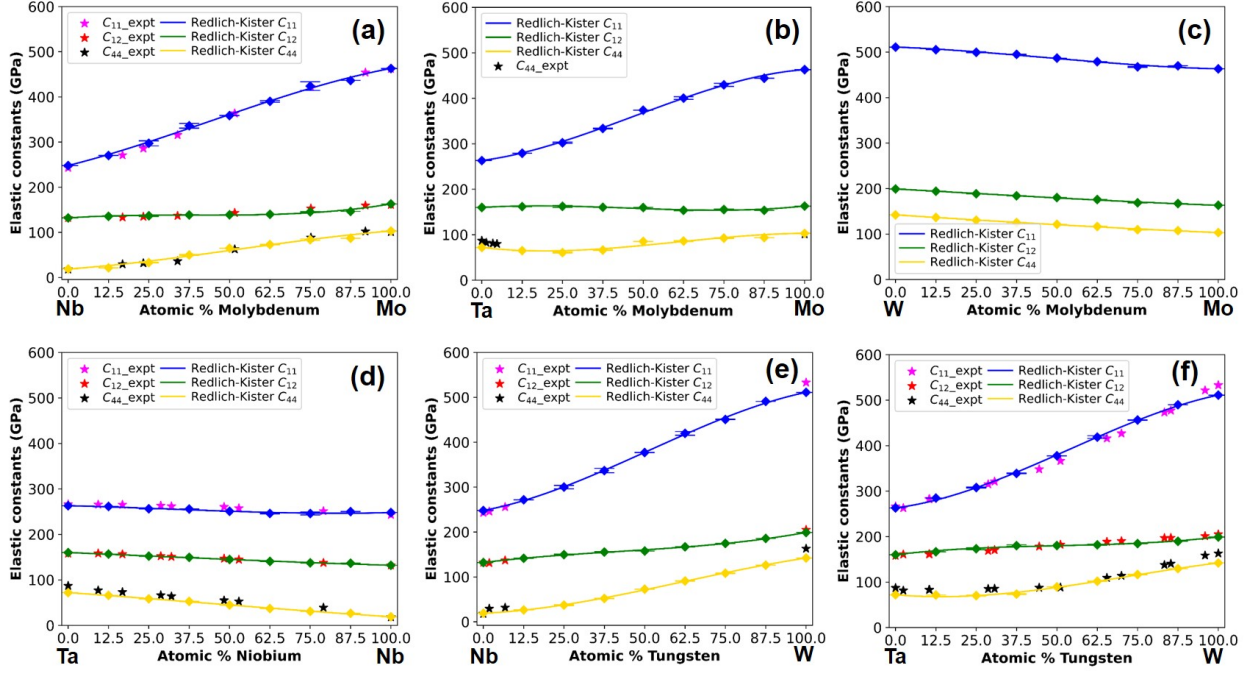


Figure 1: Composition-dependent averaged rigid-ion elastic constants  $\bar{C}_{11}^{rigid}$ ,  $\bar{C}_{12}^{rigid}$  and  $\bar{C}_{44}^{rigid}$  (solid lines, Redlich-Kister polynomial fit to computed values (filled diamonds)), compared with experimental elastic constants (stars) for (a) MoNb; (b) MoTa; (c) MoW; (d) NbTa; (e) WNb; and (f) WTa.

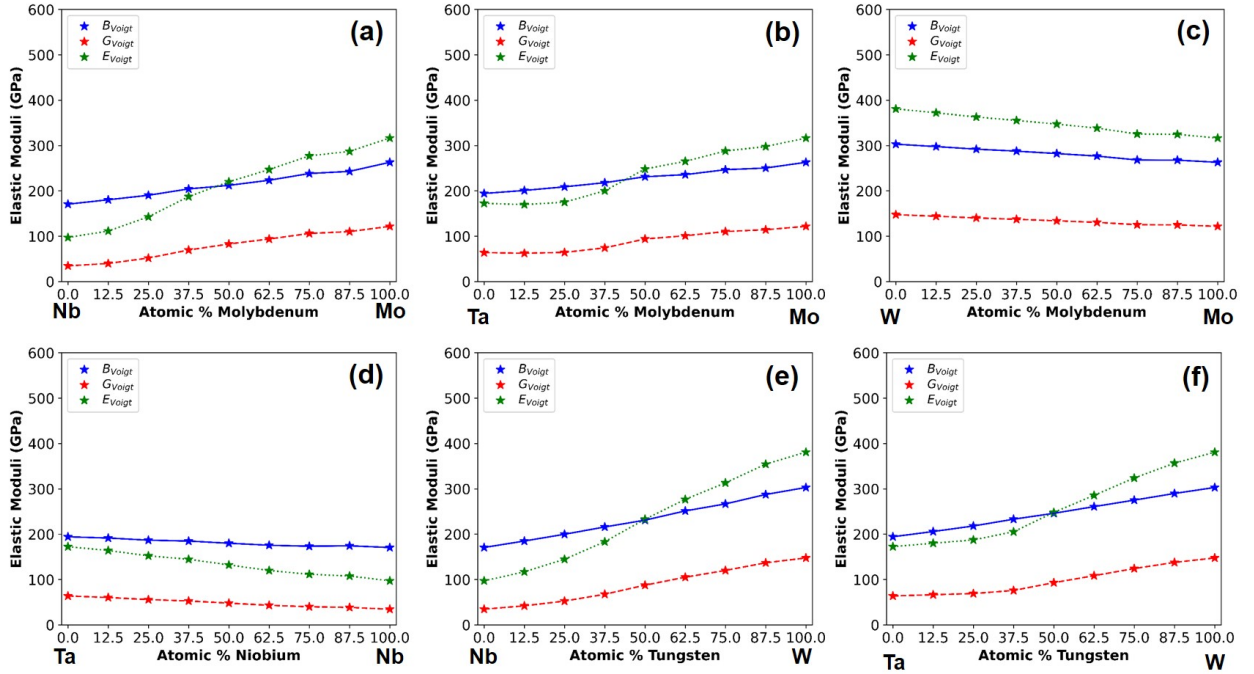


Figure 2: Composition-dependent elastic moduli  $B$ ,  $G$  and  $E$  computed using the Voigt method (Eqs. (11)–(13)), as a function of composition for (a) MoNb; (b) MoTa; (c) MoW; (d) NbTa; (e) WNb; and (f) WTa.



Table 1: Composition-dependent Voigt-averaged rigid-ion and relaxed-ion elastic constants for the binary alloys (Eq. (9)), with standard deviations ( $\pm$ ).

Composition		$\bar{C}_{11}$ (GPa)	$\bar{C}_{12}$ (GPa)	$\bar{C}_{44}$ (GPa)	$\bar{C}_{11}$ (GPa)	$\bar{C}_{12}$ (GPa)	$\bar{C}_{44}$ (GPa)
AB	at.% of A	Rigid-ion			Relaxed-ion		
MoNb	25	297.27 $\pm$ 5.5	136.83 $\pm$ 1.5	33.07 $\pm$ 0.7	294.62 $\pm$ 7.26	136.37 $\pm$ 1.63	32.05 $\pm$ 0.83
	50	358.70 $\pm$ 0.00	138.91 $\pm$ 0.00	64.91 $\pm$ 0.00	355.59 $\pm$ 0.00	138.60 $\pm$ 0.00	64.53 $\pm$ 0.00
	75	423.88 $\pm$ 9.67	145.49 $\pm$ 0.55	84.05 $\pm$ 1.43	422.56 $\pm$ 8.69	145.33 $\pm$ 0.53	83.75 $\pm$ 1.38
MoTa	25	302.24 $\pm$ 1.66	162.35 $\pm$ 2.07	60.59 $\pm$ 0.96	299.52 $\pm$ 2.50	162.19 $\pm$ 1.97	55.29 $\pm$ 0.93
	50	373.72 $\pm$ 0.00	159.89 $\pm$ 0.00	85.31 $\pm$ 0.00	369.97 $\pm$ 0.00	160.64 $\pm$ 0.00	83.17 $\pm$ 0.00
	75	429.57 $\pm$ 3.37	155.30 $\pm$ 0.90	92.48 $\pm$ 0.77	428.28 $\pm$ 3.28	155.54 $\pm$ 0.91	92.02 $\pm$ 0.76
MoW	25	499.36 $\pm$ 1.18	188.39 $\pm$ 0.15	130.25 $\pm$ 0.31	499.13 $\pm$ 1.13	188.17 $\pm$ 0.14	130.12 $\pm$ 0.28
	50	486.82 $\pm$ 0.00	180.13 $\pm$ 0.00	121.21 $\pm$ 0.00	486.38 $\pm$ 0.00	179.71 $\pm$ 0.00	120.97 $\pm$ 0.00
	75	467.32 $\pm$ 1.02	168.59 $\pm$ 0.28	109.41 $\pm$ 0.42	467.11 $\pm$ 1.02	168.39 $\pm$ 0.28	109.31 $\pm$ 0.40
NbTa	25	256.28 $\pm$ 0.66	152.21 $\pm$ 0.43	58.39 $\pm$ 0.23	256.20 $\pm$ 0.67	152.17 $\pm$ 0.40	57.20 $\pm$ 0.68
	50	250.88 $\pm$ 0.00	144.79 $\pm$ 0.00	44.68 $\pm$ 0.00	250.69 $\pm$ 0.00	144.68 $\pm$ 0.00	41.85 $\pm$ 0.00
	75	245.81 $\pm$ 3.11	137.39 $\pm$ 0.45	30.64 $\pm$ 0.27	245.70 $\pm$ 3.07	137.32 $\pm$ 0.42	28.98 $\pm$ 0.85
MoTa	25	300.06 $\pm$ 3.73	149.68 $\pm$ 1.19	37.30 $\pm$ 1.06	296.69 $\pm$ 4.22	147.89 $\pm$ 1.63	37.17 $\pm$ 1.03
	50	377.12 $\pm$ 0.00	157.79 $\pm$ 0.00	72.70 $\pm$ 0.00	371.88 $\pm$ 0.00	155.53 $\pm$ 0.00	72.46 $\pm$ 0.00
	75	450.72 $\pm$ 0.56	174.74 $\pm$ 0.34	108.10 $\pm$ 0.66	448.83 $\pm$ 1.20	173.74 $\pm$ 0.53	107.77 $\pm$ 0.56
MoW	25	307.83 $\pm$ 1.02	173.17 $\pm$ 1.97	70.16 $\pm$ 1.15	304.84 $\pm$ 1.22	171.96 $\pm$ 2.26	67.91 $\pm$ 0.46
	50	377.61 $\pm$ 0.00	180.22 $\pm$ 0.00	89.32 $\pm$ 0.00	372.38 $\pm$ 0.00	179.41 $\pm$ 0.00	88.02 $\pm$ 0.00
	75	456.06 $\pm$ 0.62	184.67 $\pm$ 0.47	116.53 $\pm$ 0.86	454.37 $\pm$ 1.93	184.27 $\pm$ 0.51	116.26 $\pm$ 0.84

compared to the Ta-containing binary alloys. In the case of the Nb-containing binary alloys MoNb and WNb, the  $B/G$  value is always less than that of the constituent elements across the entire composition range ((Figs. 3(a) and 3(e)). However, the Cauchy pressures in MoNb and WNb have higher values than those of the constituent elements at 12.5 at.% Nb composition in both binary alloys. In the case of the Ta-containing binary alloys MoTa and WTa, both  $B/G$  and the Cauchy pressure values are observed to be greater than the values for their constituent elements for some compositions (Figs. 3(b) and 3(f)). In MoTa, the  $B/G$  and Cauchy pressure values are greater than that of the ductile constituent element Ta up to  $\approx 35$  at.% and  $\approx 40$  at.% of Ta, respectively. In WTa, the  $B/G$  and Cauchy pressure values are greater than their ductile constituent element Ta up to  $\approx 37.5$  and  $\approx 52.5$  at.% of Ta, respectively.

### 3.4. Elastic field anisotropy

The finite relaxations and standard deviation values for the binary alloys summarized in Table 1 reflect different degrees of elastic anisotropy in these materials. In order to quantitate the differences among the binaries, at different compositions, we computed the  $A_G$  and  $A_E$  metrics defined in Eqs. (14) and (15). Table 2 compares the calculated anisotropies for the averaged rigid-ion elastic constants. In the case of an isotropic bulk material, these values will be unity, and the deviation from

unity corresponds to the degree of anisotropy in the material. The anisotropy measures  $A_G$  and  $A_E$  are close to one in all binary alloys, corresponding to near-isotropic behavior. These anisotropies reflect the local anisotropy at the atomic level, corresponding to different atomic bond strengths in different crystallographic planes. Although the values of  $A_G$  and  $A_E$  suggest that the binary alloys are near-isotropic, these measures do not provide insight into the spatial variations of the elastic moduli. Together with  $A_G$  and  $A_E$ , we therefore define a new metric,  $A_G^R$ , the shear anisotropy due to nuclear-relaxation contributions to the shear modulus  $A_G^R$ :

$$A_G^R = 1 - \frac{\bar{G}^{\text{nuclear}}}{\bar{G}^{\text{relaxed}}}. \quad (21)$$

The values of  $A_G^R$  are also listed in Table 2.

To further analyze the extent of elastic tensor property anisotropy in the refractory binary alloys, 3D plots of the orientation-dependent  $G$ ,  $E$  and  $\nu$ , for three compositions each, were generated using the ELATE tool [106]. The results for MoNb and WTa are shown in Figs. 4 and 5; the results for MoTa, MoW, NbTa, and WNb can be found in the Appendix. The axes of the 3D plots in the figures correspond to the crystal orientations  $[100]$ ,  $[010]$ ,  $[001]$  in the  $x$ ,  $y$ , and  $z$  directions, respectively. The maximum and minimum values of  $G$  and  $\nu$  are represented as transparent blue and solid green surfaces. The extent of anisotropy is seen to be greatest for MoNb. For the Young's modulus  $E$ ,

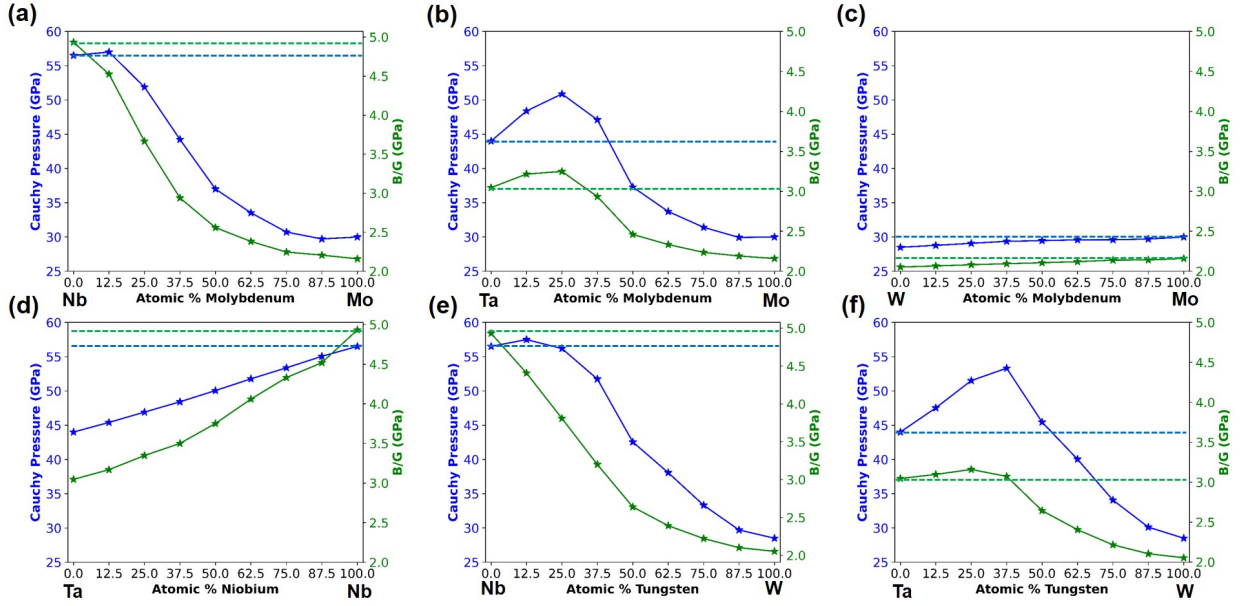


Figure 3: Composition-dependent Pugh's ratio ( $B/G$ ; green) and Cauchy pressure ( $(C_{12} - C_{44})$ ; blue) for (a) MoNb; (b) MoTa; (c) MoW; (d) NbTa; (e) WNb; and (f) WTa. Horizontal lines indicate maximum Cauchy pressure or Pugh's ratio of the constituent elements.

Table 2: Comparison of  $A_G$  (Eq. (14)),  $A_E$  (Eq. (15)) and  $A_G^R$  (Eq. (21)) for all binary alloys and different compositions.

Composition		$A_G$	$A_E$	$A_G^R$	Composition		$A_G$	$A_E$	$A_G^R$
AB	at.% of A				AB	at.% of A			
MoNb	25	1.024	1.038	0.979	MoTa	25	1.007	0.987	0.939
	50	1.000	1.000	0.991		50	1.000	1.000	0.977
	75	0.984	0.959	0.996		75	0.996	1.015	0.995
MoW	25	1.000	1.000	0.999	NbTa	25	1.009	1.003	0.986
	50	1.000	1.000	0.999		50	1.000	1.000	0.961
	75	1.001	1.003	1.000		75	1.013	1.004	0.973
WNb	25	0.982	0.970	0.992	WTa	25	0.999	1.000	0.991
	50	1.000	1.000	0.992		50	1.000	1.000	0.993
	75	0.997	1.004	0.997		75	0.995	1.004	0.994

$\langle 100 \rangle$  is the stiffest direction and  $\langle 111 \rangle$  is the most compliant direction in all compositions of the binary alloys except for  $\text{Nb}_{0.25}\text{Ta}_{0.75}$  and  $\text{W}_{0.25}\text{Ta}_{0.75}$ , which have nearly perfect spherical shapes, corresponding to elastic isotropy.  $\text{Mo}_{0.25}\text{Nb}_{0.75}$ ,  $\text{W}_{0.25}\text{Nb}_{0.75}$  and  $\text{Nb}_{0.75}\text{Ta}_{0.25}$  deviate strongly away from spherical, indicating high elastic anisotropy. Interestingly, WTa exhibits near-isotropic behavior at all compositions as seen in Fig. 5. Similar trends are observed for  $G$  and  $\nu$ . The patterns observed in the 3D plots are consistent with the reduced metrics  $A_E$  and  $A_G$  in Table 2. For  $A_E$ , all binaries showed near-isotropic behavior with deviations away from 1 of  $\leq 1\%$  except for  $\text{Mo}_{0.25}\text{Nb}_{0.75}$ ,  $\text{Mo}_{0.75}\text{Nb}_{0.25}$  and  $\text{W}_{0.25}\text{Nb}_{0.75}$ , where the deviations are  $> 3\%$ . For

$A_G$ , all binaries exhibited near-isotropic behavior (deviations of  $< 1\%$ ), except for  $\text{Mo}_{0.25}\text{Nb}_{0.75}$ ,  $\text{Mo}_{0.75}\text{Nb}_{0.25}$ ,  $\text{Nb}_{0.75}\text{Ta}_{0.25}$  and  $\text{W}_{0.25}\text{Nb}_{0.75}$ , which exhibit greater deviations away from unity.

### 3.5. Nuclear-relaxation contributions to elastic properties

The method employed in computing the nuclear-relaxation contributions to the elastic tensor makes it possible to decompose it into atom-specific contributions, allowing more detailed modeling of the microscopic origins of elastic response in the binary alloys. The force response internal strain tensor  $\Lambda_n^\alpha$  characterizes the force response of atom  $\alpha$  along direction  $n$  (in

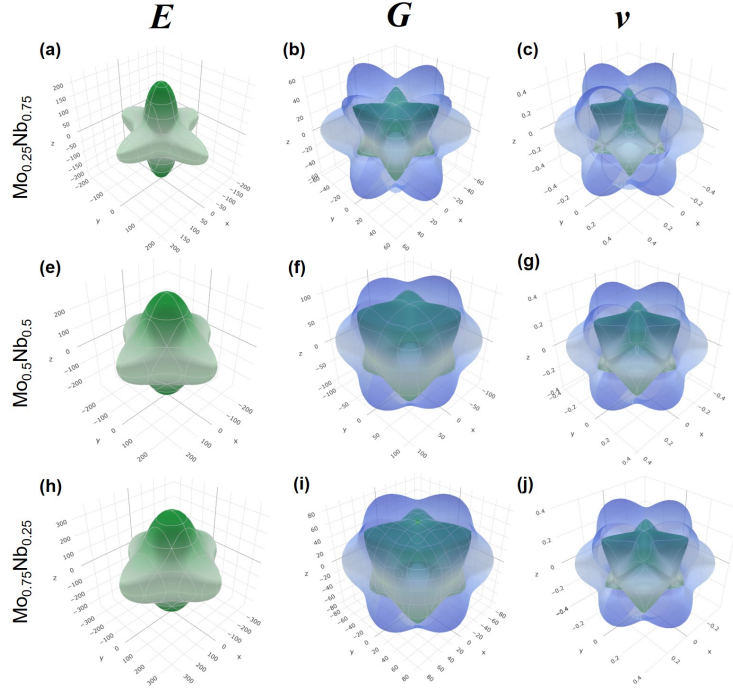


Figure 4: Spatial dependence of  $G$  (GPa),  $E$  (GPa), and  $\nu$  for: (a)-(c)  $\text{Mo}_{0.25}\text{Nb}_{0.75}$ ; (d)-(f)  $\text{Mo}_{0.5}\text{Nb}_{0.5}$ ; and (g)-(h)  $\text{Mo}_{0.75}\text{Nb}_{0.25}$ . Plots generated using the ELATE tool [106]. The maximum and minimum values of  $G$ ,  $E$  and  $\nu$  are represented as transparent blue and solid green surfaces respectively.

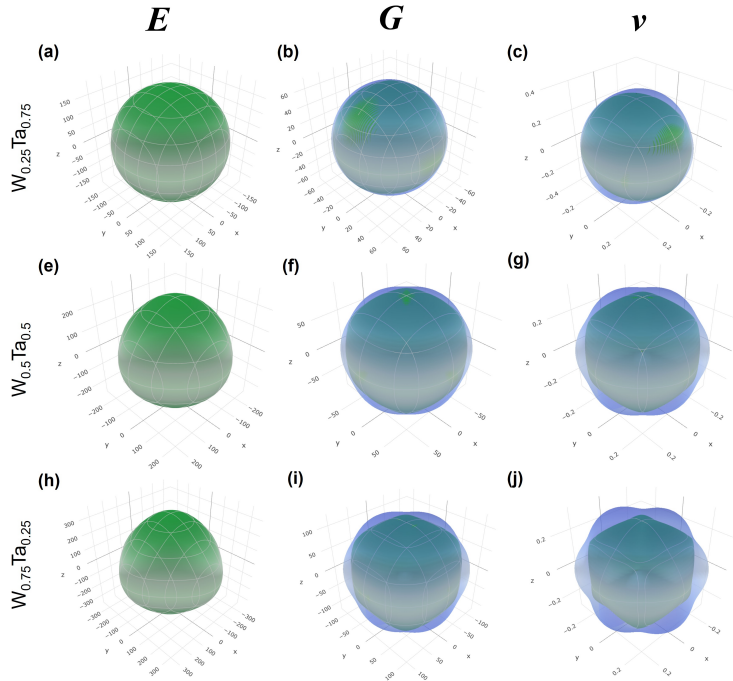


Figure 5: Spatial dependence of  $G$  (in GPa),  $E$  (in GPa), and  $\nu$  for: (a)-(c)  $\text{W}_{0.25}\text{Ta}_{0.75}$ ; (d)-(f)  $\text{W}_{0.5}\text{Ta}_{0.5}$ ; and (g)-(h)  $\text{W}_{0.75}\text{Ta}_{0.25}$ . Plots generated using the ELATE tool [106]. The maximum and minimum values of  $G$ ,  $E$  and  $\nu$  are represented as transparent blue and solid green surfaces respectively.

Voigt notation) to the internal strain, while the displacement response internal strain tensor  $\Gamma_n^\alpha$  characterizes the displacement response of the atom  $\alpha$  along direction  $n$  to the internal strain. The product of these intermediate values summed over all directions for a given atom  $\alpha$  gives the relaxation value of a given elastic constant or shear modulus  $G$  of atom  $\alpha$  under macroscopic strain (Eqs. (16) and (17)). To illustrate the resulting spatial variation in a relaxed crystal structure, the relaxation effects are displayed as contour plots in Figs. 6-7 for NbTa and WTa, and for MoNb, MoTa, MoW, and WTa in the Appendix. The supercell is represented as a set of  $\langle 001 \rangle$  planes. A supercell with unit cells stacked in  $2 \times 2 \times 2$  fashion has 4 unique  $\langle 001 \rangle$  planes. These are used to construct 2D layers in order to represent the 3D periodic supercell. Each layer contains the atoms of their respective  $\langle 001 \rangle$  plane, and their first nearest neighbors (1NN) from the next plane. For example, layer 1 consists of atoms from the plane 1 and atoms from plane 2 (these are the 1NN of the atoms in plane 1) projected onto plane 1. Interpolation between atomic contributions is used to construct the spatially-dependent relaxation field [107] for each elastic tensor quantity, using a linear function. The color bar in the contour plot has a range varying from minimum (blue) to maximum (yellow) relaxation value.

In the case of NbTa (Fig. 6), the constituent elements Nb and Ta have similar single-bond covalent atomic radii ( $r_{\text{cov}} = 1.47 \text{ \AA}$  for Nb and  $1.46 \text{ \AA}$  for Ta [108]), and exhibit a small difference in their elastic constants. The relaxation values of the Nb atoms and Ta atoms vary with lattice position for  $\bar{C}_{11}$ ,  $\bar{C}_{12}$ ,  $\bar{C}_{44}$  and  $G$ . This is due to differences in the surrounding atoms at each lattice site, which is the nature of disordered systems. The average relaxation value of a Nb atom for  $\bar{C}_{11}$ ,  $\bar{C}_{12}$ ,  $\bar{C}_{44}$  and  $G$  in case of  $\text{Nb}_{0.25}\text{Ta}_{0.75}$ , where Nb atom is the alloying element, is lower than that of the host Ta atoms. Similarly, the average relaxation value of the Ta atom for  $\bar{C}_{11}$ ,  $\bar{C}_{12}$ ,  $\bar{C}_{44}$  and  $G$  for  $\text{Nb}_{0.75}\text{Ta}_{0.25}$ , where the Ta atom is alloying element, is lower than that of the host Nb atoms. The distribution of atomic relaxation values for  $\text{Nb}_{0.25}\text{Ta}_{0.75}$  and  $\text{Nb}_{0.75}\text{Ta}_{0.25}$  are similar for  $\bar{C}_{11}$ ,  $\bar{C}_{12}$ ,  $\bar{C}_{44}$  and  $G$ , but different for  $\text{Nb}_{0.5}\text{Ta}_{0.5}$ , with no common trend observed among  $\bar{C}_{11}$ ,  $\bar{C}_{12}$ ,  $\bar{C}_{44}$  and  $G$ .

Fig. 7 shows the decompositions of relaxation values in WTa, for which the constituent elements W and Ta have different single-bond covalent atomic radii ( $r_{\text{cov}} = 1.37 \text{ \AA}$  for W and  $1.46 \text{ \AA}$  for Ta [108]), and significant differences in their elastic constants. As for NbTa, the relaxation values of the W and Ta atoms vary with lattice position for  $\bar{C}_{11}$ ,  $\bar{C}_{12}$ ,  $\bar{C}_{44}$  and  $G$ . Similar to NbTa, the average relaxation value of the W atoms is lower for

$\bar{C}_{11}$ ,  $\bar{C}_{44}$  and  $G$  in the case of  $\text{W}_{0.25}\text{Ta}_{0.75}$  when W is the alloying element, and the average relaxation value of the Ta atoms is lower for  $\bar{C}_{11}$ ,  $\bar{C}_{44}$  and  $G$  in case of  $\text{W}_{0.75}\text{Ta}_{0.25}$  when Ta is the alloying element. However, for  $\bar{C}_{12}$  of WTa, the average relaxation value of the W atoms is greater when W is the alloying element ( $\text{W}_{0.25}\text{Ta}_{0.75}$ ) and the average relaxation value of the Ta atoms is greater in  $\text{W}_{0.75}\text{Ta}_{0.25}$ , where Ta is alloying element.

### 3.6. Computational efficiency of DFPT vs. stress-strain methods

In order to assess the computational efficiency of DFPT for computing the elastic tensor vs. stress-strain methods, we computed  $B$  for  $\text{Mo}_{0.25}\text{Nb}_{0.75}$  as an exemplar system, using a 16-atom SQS supercell and the stress-strain method as described by the Materials Project [55]. The DFT computational parameters and atomic configuration were the same as used in the DFPT calculations for this binary. In the stress-strain method,  $B$  is determined by applying an equal strain along the  $x$ ,  $y$ , and  $z$  directions for each of four different strain magnitudes, without allowing atomic relaxation; this mimics the rigid-ion method of the present work. The resulting stress-strain-computed  $B$  for  $\text{Mo}_{0.25}\text{Nb}_{0.75}$  is 190.3 GPa, in excellent agreement with the rigid-ion-computed  $B$ , 189.9 GPa. As discussed earlier, a total of 24+1 DFT calculations were required in order to compute the complete elastic tensor for determining  $B$ .

By comparison, the computation of the elastic tensor using DFPT required only one calculation once the relaxed structures for the rigid-ion and relaxed-ion elastic tensors had been obtained. Computation of the rigid-ion elastic tensor is faster than the computation of the relaxed structure; hence, the total time needed for computing the rigid-ion elastic tensor is less than the time required to perform two independent computations. By contrast, the stress strain-method requires 25 independent computations. In case of the relaxed-ion method, the total time for the computation is greater than for the rigid-ion method, as the energy derivatives with respect to the atomic displacements for all atoms are needed.

An alternative method for computing the elastic tensor utilizes a finite-difference approach to compute the necessary energy derivatives. Numerical validation of the DFPT compared to finite difference methods has been done previously [63, 68, 109]. In the finite difference approach, a minimum of 5 DFT computations are needed in order to compute each independent elastic constant using a 5-point derivative formula. Martin *et al.* [68] investigated the computational efficiency of DFPT for computing the elastic tensor of  $\text{Fe}_{16}\text{C}$

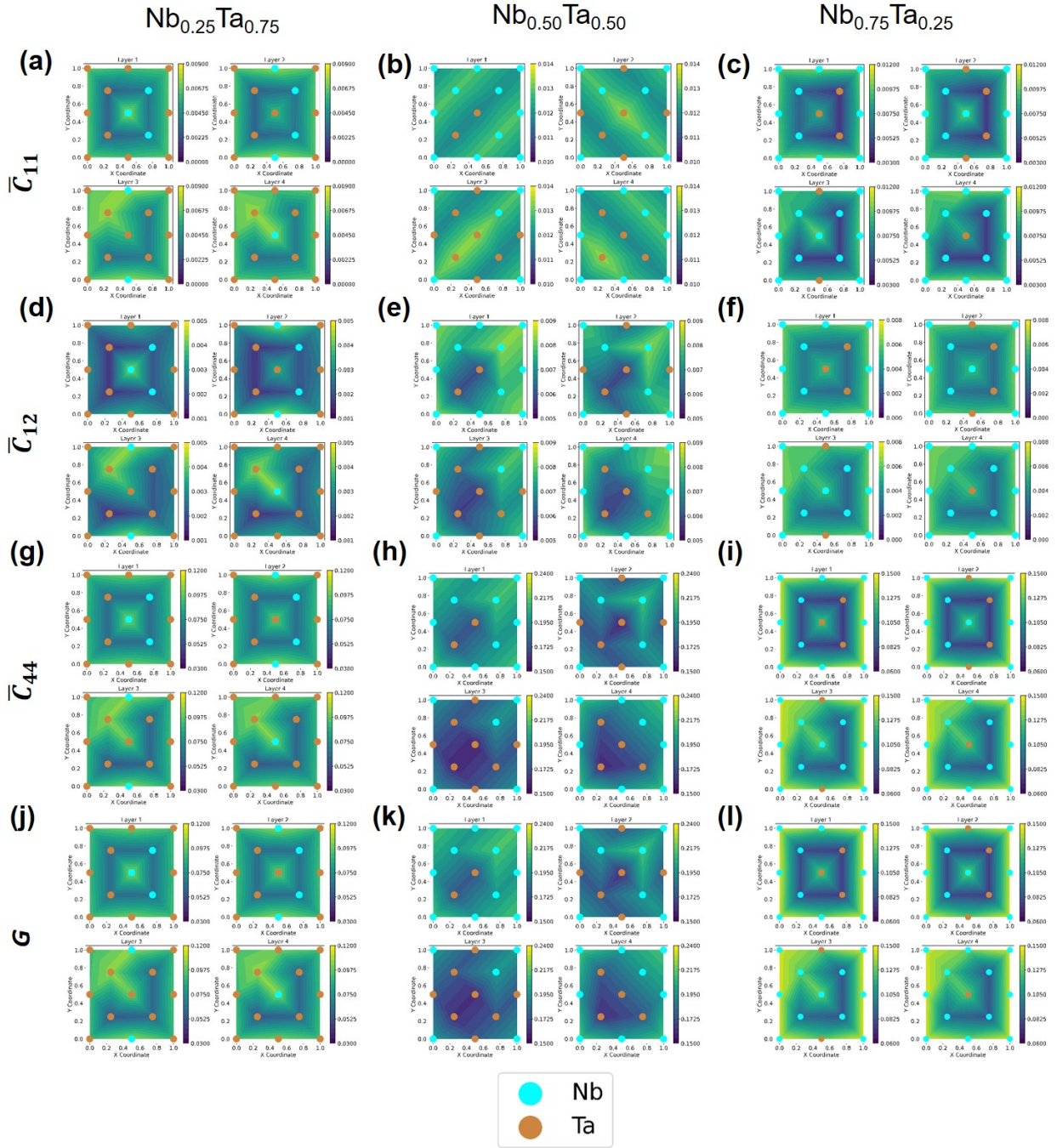


Figure 6: Relaxation field (values in GPa) constructed as described in text for  $Nb_{0.25}Ta_{0.75}$ ,  $Nb_{0.5}Ta_{0.5}$ , and  $Nb_{0.75}Ta_{0.25}$ . (a)-(c):  $\bar{C}_{11}$ , (d)-(f):  $\bar{C}_{12}$ , (g)-(i):  $\bar{C}_{44}$ , and (j)-(l):  $G$ . The color bar is set to range from minimum to maximum relaxation values for all atoms.  $x$  and  $y$  coordinates correspond to reduced coordinates in the 3D supercell.

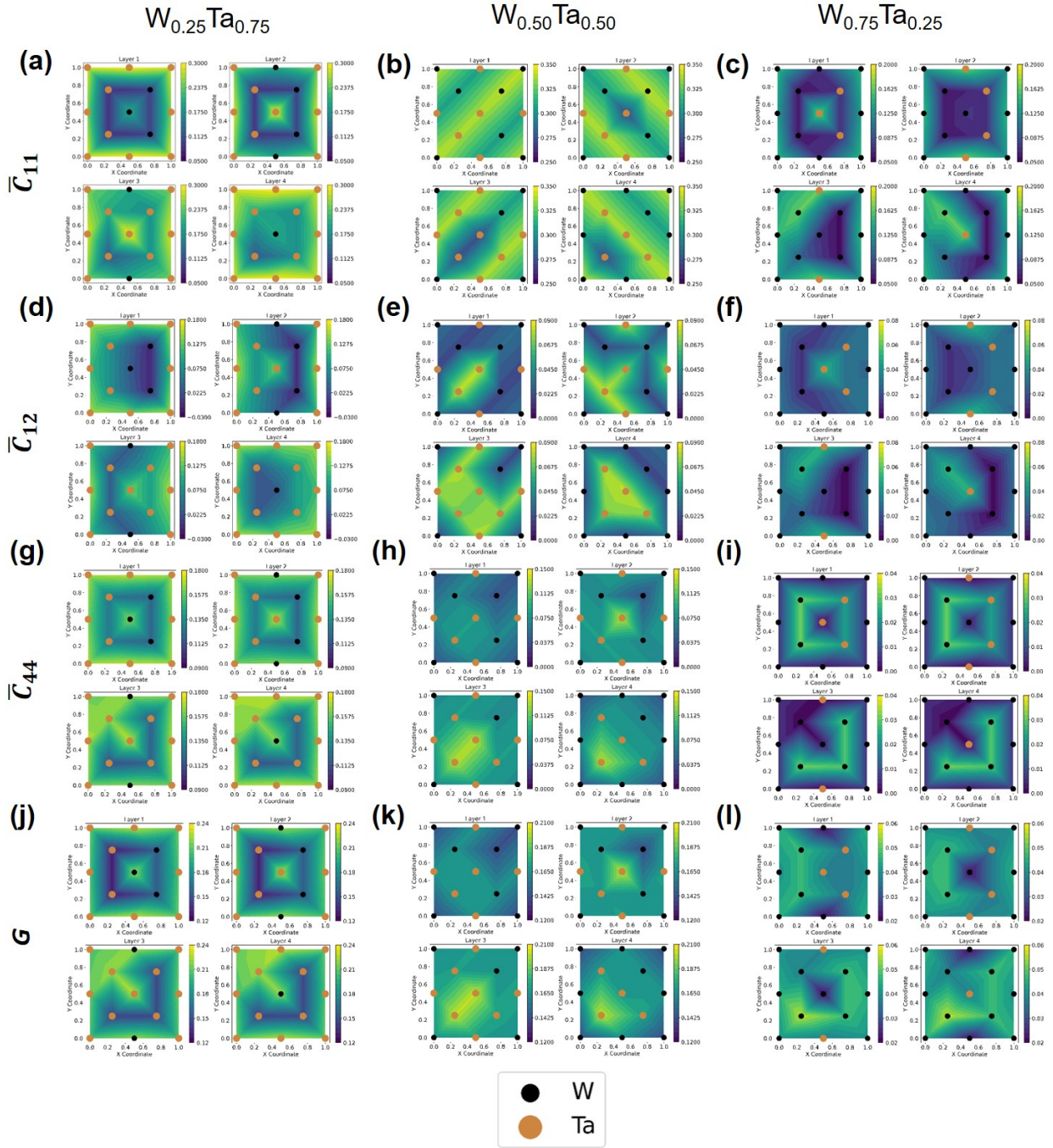


Figure 7: Relaxation field (values in GPa) constructed as described in text for  $W_{0.25}Ta_{0.75}$ ,  $W_{0.50}Ta_{0.50}$ , and  $W_{0.75}Ta_{0.25}$ . (a)-(c):  $\bar{C}_{11}$ , (d)-(f):  $\bar{C}_{12}$ , (g)-(i):  $\bar{C}_{44}$ , and (j)-(l):  $G$ . The color bar is set to range from minimum to maximum relaxation values for all atoms.  $x$  and  $y$  coordinates correspond to reduced coordinates in the 3D supercell.

with trigonal symmetry and seven independent elastic constants, using a PAW pseudopotential. They found that DFPT was  $18.5\times$  faster than the finite difference approach. In our calculations for  $\text{Mo}_{0.25}\text{Nb}_{0.75}$ , we found that the rigid-ion method was  $17.7\times$  faster and the relaxed-ion method was  $5.1\times$  faster than the stress-strain method.

## 4. Discussion

### 4.1. Elastic tensor variations with distortions in lattice

Within continuum elasticity theory [90], the ideal elastic tensor of a cubic crystal (including BCC) has only three independent elastic constants due to the lattice symmetry of the crystal. The number of independent elastic constants will increase when the symmetry of the crystal is broken. Alloying introduces distortions in the perfect lattice due to differences in the atomic radii and quantum mechanical interactions between the constituent atoms [35]. This causes lattice distortions and introduces local strain, which hinders dislocation motion, thus increasing the mechanical strength [17, 110]. Hence it is crucial to correlate the effects of distortions on the elastic tensor due to alloying, and develop computational methods for characterizing these effects at the microscopic level.

To understand the effect of distortions on the the elastic constants we define two types of distortions, crystal distortions and lattice distortions. Crystal distortions correspond to changes in the lattice parameter in different directions due to symmetry breaking of the BCC crystal. Lattice distortions refer to atomic motion away from ideal lattice sites due to differences in the electronic (quantum mechanical) interactions between the atoms. Computation of the relaxed-ion elastic tensor using DFPT, instead of computing only  $C_{11}$ ,  $C_{12}$  and  $C_{44}$ , makes it possible to capture crystal distortions and lattice distortions in terms of standard deviations in Voigt averages and nuclear relaxation values in the BCC binary alloys. Non-zero standard deviation values in the Voigt-averaged elastic constants signal crystal distortions  $a_x \neq a_y \neq a_z$ . In the case of  $A = 50$  at.% composition in the AB binary alloys, the relaxed structures retain cubic crystal symmetry ( $a_x = a_y = a_z$ ), leading to  $C_{11} = C_{22} = C_{33}$ ,  $C_{12} = C_{23} = C_{31}$  and  $C_{44} = C_{55} = C_{66}$ , and thus a zero standard deviation in the Voigt-averaged values. Nevertheless, although crystal symmetry is preserved in the 50-50 binary alloys, deviations away from the perfect lattice are still possible, and indeed, these can play an important role in determining the mechanical behavior of high-entropy alloys [111].

Lattice distortions in the relaxed structure of the binary alloys lead to unbalanced forces on the crystal under a finite strain as illustrated schematically in Fig. 8. The magnitude and direction of resultant unbalanced forces at each lattice site depends on the atom type and the atomic environment in the lattice. In disordered binary alloys, atom type and atomic environment differ at each lattice site. Nuclear relaxation values, which contribute to the computation of relaxed-ion elastic constants, provides the measure of resultant unbalanced forces in the crystal under finite strain. While standard deviation values for the binary alloys with  $A = 50$  at.% is zero, indicating cubic crystal structure, the nuclear relaxation values are non-zero and are maximum for  $\bar{C}_{11}$ . This indicates that in  $A = 50$  at.% binary alloys, even though there are no crystal distortions, there are lattice distortions in the crystal which lead to unbalanced forces in the crystal. For same-group binary alloys,  $\bar{C}_{11}$ ,  $\bar{C}_{12}$  and  $\bar{C}_{44}$  are observed to be close to zero indicating minute lattice distortions except for  $\bar{C}_{44}$  of NbTa. For  $\bar{C}_{44}$  of NbTa, the nuclear relaxation values are finite even though the standard deviation values are zero. This indicates that, in NbTa, the unbalanced forces are oriented in a particular direction as only  $\bar{C}_{44}$  has a finite contribution, while  $\bar{C}_{11}$  and  $\bar{C}_{12}$  has near-zero contributions. Even though on the macroscopic scale, no crystal distortions are observed, at the microscopic scale the unbalanced forces are oriented in a particular direction, which reduces the magnitude of relaxed-ion elastic constants. In case of MoW and NbTa, nuclear relaxation values are near zero (except for  $\bar{C}_{44}$  of NbTa) for all compositions, while the standard deviation values are finite for  $A = 25$  at.% and  $50$  at.% compositions. This may be due to near-zero unbalanced forces on the atoms under strain or random orientation of the forces on the atoms resulting in near-zero overall relaxation values.

### 4.2. Effect of alloying on elastic properties

The input structures used in the DFPT rigid-ion and relaxed-ion calculations can impact the accuracy of the final computed elastic tensors, through residual stresses. In principle, it is possible to correct for any initial stresses present in the starting structure [47]. In the present work, we have utilized fully-relaxed input SQS supercell structures in order to avoid the need for *ex post facto* corrections and to maintain internal consistency in our calculations. The input structures are obtained for each binary and composition by minimizing the forces on each atom, allowing cell shape, dimensions and relative atomic positions on the lattice to vary. The particular computational procedures followed here

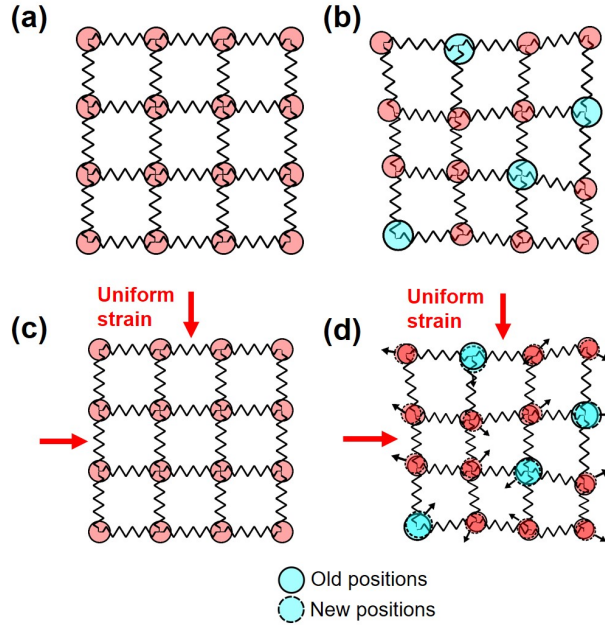


Figure 8: Resultant forces on atoms under uniform strain in unary and binary alloys. (a) Bulk crystal in relaxed state; (b) binary alloy in relaxed state; (c) bulk crystal in strain state; and (d) binary alloy in strain state. Here dashed circles represent the new position of atoms in a strained crystal in its relaxed state. Red arrows indicates the deformation direction; black arrows indicate resultant forces on the atoms.

have been essential to obtaining elastic constants in remarkably good agreement with experiment.

Elastic constants are fundamental probe of the elastic interactions of atoms in a given material and are correlated with mechanical properties. Due to random arrangement of atoms in disordered alloys, the elastic interactions are complex and difficult to quantify. In single crystal disordered alloys, solid solution effects like solid solution strengthening are the major contributing factors to observed changes in mechanical properties due to alloying. Since the seminal works of Fleisher [112] and Labusch [113], solid solution effects have been correlated with differences in atomic radii and elastic moduli. The fundamental idea behind this is to capture the lattice distortions and associated local strains due to alloying [114, 115]. Even though these models have been widely verified for yield strength, they can be used to understand trends in elastic constants as well [116, 117]. For same-group binary alloys (MoW and NbTa), the differences in single-bond covalent atomic radii and differences in shear moduli of the constituent elements are smaller compared to those of different-group elements. Hence same-group alloys showed a linear trend across the entire composition range for  $\bar{C}_{11}$ ,  $\bar{C}_{12}$  and  $\bar{C}_{44}$ , closely following Vegard's law. However, in different-group binary alloys (MoNb,

MoTa, WNb and WTa) the differences in atomic radii and differences in shear moduli of the constituent elements lead to nonlinear trends, with deviations from Vegard's law.

#### 4.3. Nuclear relaxation contributions to the elastic tensor

Nuclear-relaxation contributions to the elastic constants capture the influence of atomic rearrangement caused by alloying. These can be physically interpreted as a measure of resultant unbalanced forces on the atoms due to lattice distortions when the crystal is under strain. Relaxation values corresponding to different elastic constants describe relaxation effects in a particular direction of the atoms under strain. In disordered random alloys, the chemical randomness at each lattice site leads to differences in relaxation values at each lattice site. This value is subtracted from the rigid-ion elastic constant values, which are uniform in a crystal, in order to obtain the physical elastic constants. Hence relaxation values provide a measure of heterogeneity in elastic constants.

The elastic constant trends showed deviations from Vegard's law in case of different-group binary alloys. A positive deviation (value greater than value computed using Vegard's law) is seen in the compositions with



higher atomic fraction of the constituent element with higher elastic constant value in the case of  $\bar{C}_{11}$  and  $\bar{C}_{44}$ , while an inverse trend is found for  $\bar{C}_{12}$ . In case of different-group binary alloys, average relaxation values for alloying element is lower than the average relaxation values of the host element for  $\bar{C}_{11}$  and  $\bar{C}_{44}$ . For  $\bar{C}_{12}$  the trend is exactly opposite, similar to the trends in deviations from Vegard's law.

Elastic constants are fundamental probes of the nature of bonding in a given material. Elastic constant heterogeneity provides a direct measure of varying bond strength in alloys. Higher relaxation values lead to lower elastic constant values, as relaxation values are subtracted from the rigid-ion elastic constants. This effect plays a crucial role in understanding the location of a crack's initial site in disordered alloys, as locations with higher relaxation values will have lower elastic constants, hence higher stress concentration sites, thus serving as crack initiation sites. The methodology adopted here can be easily extended to multi-component systems where the relaxation values are expected to be even higher due to larger lattice distortions [118].

## 5. Conclusions

In this work, the elastic tensors of composition-dependent refractory binary alloys based on Mo, Nb, Ta, and W have been computed at a high level of quantum mechanical theory using density functional perturbation theory in conjunction with SQS supercell modeling of the composition-dependent disordered BCC structures. Both the rigid-ion and relaxed ion elastic tensors were computed. The Voigt-averaged elastic constants  $\bar{C}_{11}$ ,  $\bar{C}_{12}$ , and  $\bar{C}_{22}$  derived from the elastic tensors were used to compute the polycrystalline elastic moduli  $E$ ,  $B$ , and  $G$ . Relaxed-ion calculations for the elastic constants corresponding to the inclusion of nuclear relaxation effects under uniform strain are consistent with experiment. Differences between the rigid-ion and relaxed-ion values for the elastic constants were found to lie within the standard deviations of their Voigt averages for the 25, 50, and 75 at.% alloy compositions, suggesting that nuclear relaxation contributions to the elastic tensor are relatively small. This made it possible to extend rigid-ion elastic tensor and derived elastic properties to additional alloy compositions with no loss in accuracy. The computed rigid-ion elastic constants are in excellent agreement with available experimental data, demonstrating the ability of our methodology to accurately predict key mechanical properties from first-principles theory. Derived mechanical properties of  $B$ ,  $G$  and  $E$  showed a linear trend in properties across the

compositions for same-group binary alloys and a non-linear trend in different-group binary alloys. Our calculations showed elastic anisotropy behavior in all of the binary alloys except WTa.

In addition to the ability to neglect nuclear relaxation contributions in computing accurate mechanical properties for the considered alloys, we compared our approach to conventional stress-strain methods, and found that accurate results can be obtained with an order of magnitude reduction in computational cost. For the test system of  $\text{Mo}_{0.25}\text{Nb}_{0.75}$ , the rigid-ion DFPT calculation of  $B$  was in exact agreement with the results of conventional stress-strain approach. Even though the relaxation values are small, the decomposition of the elastic constants into electronic contributions and nuclear relaxation contributions helped to understand the effects of nuclear relaxations on the symmetry of the elastic tensor. Computation of relaxation values allowed to map the heterogeneity in elastic constants which can play a crucial role in understanding crack initial site in disordered alloys. The ability to perform reliable high-throughput calculations will make it possible to establish accurate property databases for microscopic modeling of the mechanical properties of compositionally- and chemically-complex alloys.

## Acknowledgements

This work was supported in part by NASA EPSCoR Grant # 80NSSC21M0171. We would like to thank the UNM Center for Advanced Research Computing, supported in part by the National Science Foundation, for providing computational resources and system support for this work.

## References

- [1] G. E. Dieter, D. Bacon, Mechanical Metallurgy, Vol. 3, McGraw-Hill, New York, 1976.
- [2] H. Chen, A. Kauffmann, S. Laube, I.-C. Choi, R. Schwaiger, Y. Huang, K. Lichtenberg, F. Müller, B. Gorr, H.-J. Christ, et al., Contribution of lattice distortion to solid solution strengthening in a series of refractory high entropy alloys, *Metallurgical and Materials Transactions A* 49 (2018) 772–781.
- [3] M. Walbrühl, D. Linder, J. Ågren, A. Borgenstam, Modelling of solid solution strengthening in multicomponent alloys, *Materials Science and Engineering: A* 700 (2017) 301–311.
- [4] S. T. Bijjala, R. Wilkerson, C. Beamer, P. Kumar, Understanding the phase evolution and elemental distribution in  $\text{MoWTaNbVTi}_x$  manufactured via powder metallurgical approach, *The International Journal of Advanced Manufacturing Technology* (2024) 1–19.
- [5] J.-C. Liang, X.-W. Li, J.-C. Wu, Z.-X. Wei, X.-L. Wang, First-principles study on structural stability, electronic structure and mechanical properties of VB group transition metal tungsten

- alloys W-TM (TM = V, Nb, Ta), *Materials Today Communications* 38 (2024) 107920.
- [6] C. Marker, S.-L. Shang, J.-C. Zhao, Z.-K. Liu, Effects of alloying elements on the elastic properties of bcc Ti-X alloys from first-principles calculations, *Computational Materials Science* 142 (2018) 215–226.
  - [7] M. Muzyk, D. Nguyen-Manh, K. Kurzydłowski, N. Baluc, S. Dudarev, Phase stability, point defects, and elastic properties of W-V and W-Ta alloys, *Physical Review B* 84 (10) (2011) 104115.
  - [8] W. P. Huhn, M. Widom, A. M. Cheung, G. J. Shiflet, S. J. Poon, J. Lewandowski, First-principles calculation of elastic moduli of early-late transition metal alloys, *Physical Review B* 89 (10) (2014) 104103.
  - [9] R. Hill, The elastic behaviour of a crystalline aggregate, *Proceedings of the Physical Society. Section A* 65 (5) (1952) 349.
  - [10] N. Bouarissa, K. Kassali, Mechanical properties and elastic constants of zinc-blende  $\text{Ga}_{1-x}\text{In}_x\text{N}$  alloys, *Physica Status Solidi (b)* 228 (3) (2001) 663–670.
  - [11] O. De la Peña-Seaman, R. De Coss, R. Heid, K.-P. Bohnen, Ab initio study of the structural, electronic, and phononic properties of  $\text{Nb}_{1-x}\text{Mo}_x$  using the self-consistent virtual-crystal approximation, *Physical Review B* 76 (17) (2007) 174205.
  - [12] C. Laberge, P. Fratzl, J. Lebowitz, Elastic effects on phase segregation in alloys with external stresses, *Physical Review Letters* 75 (24) (1995) 4448.
  - [13] J. Zhang, Z. Chen, Y. X. Wang, Y. L. Lu, Effects of elastic strain energy on the antisite defect of  $\text{D}_{022}\text{-Ni}_3\text{V}$  phase, *Physica B: Condensed Matter* 405 (1) (2010) 140–144.
  - [14] M. Born, On the stability of crystal lattices. I, *Mathematical Proceedings of the Cambridge Philosophical Society* 36 (1940) 160–172.
  - [15] M. Born, K. Huang, *Dynamical Theory of Crystal Lattices*, Oxford University Press, New York, 1954.
  - [16] K. Persson, M. Ekman, G. Grimvall, Dynamical and thermodynamical instabilities in the disordered  $\text{Re}_x\text{W}_{1-x}$  system, *Physical Review B* 60 (14) (1999) 9999.
  - [17] O. Senkov, G. Wilks, D. Miracle, C. Chuang, P. Liaw, Refractory high-entropy alloys, *Intermetallics* 18 (9) (2010) 1758–1765.
  - [18] O. N. Senkov, D. B. Miracle, K. J. Chaput, J.-P. Couzinie, Development and exploration of refractory high entropy alloys—a review, *Journal of Materials Research* 33 (19) (2018) 3092–3128.
  - [19] G. Ouyang, P. Singh, R. Su, D. D. Johnson, M. J. Kramer, J. H. Perepezko, O. N. Senkov, D. Miracle, J. Cui, Design of refractory multi-principal-element alloys for high-temperature applications, *npj Computational Materials* 9 (1) (2023) 141.
  - [20] S. Pugh, XCII. Relations between the elastic moduli and the plastic properties of polycrystalline pure metals, *The London, Edinburgh, and Dublin Philosophical Magazine and Journal of Science* 45 (367) (1954) 823–843.
  - [21] D. Pettifor, Theoretical predictions of structure and related properties of intermetallics, *Materials Science and Technology* 8 (4) (1992) 345–349.
  - [22] A. Cottrell, *Advances in Physical Metallurgy: A Collection of Invited Papers Presented to Mark the 70th Birthday Year of Professor Sir Alan Cottrell*, Vol. 495, CRC Press, 1990.
  - [23] M. C. Gao, Ö. N. Doğan, P. King, A. D. Rollett, M. Widom, The first-principles design of ductile refractory alloys, *JOM* 60 (2008) 61–65.
  - [24] R. Feng, G. Kim, D. Yu, Y. Chen, W. Chen, P. K. Liaw, K. An, Elastic behavior of binary and ternary refractory multi-principal-element alloys, *Materials & Design* 219 (2022) 110820.
  - [25] H. Niu, X.-Q. Chen, P. Liu, W. Xing, X. Cheng, D. Li, Y. Li, Extra-electron induced covalent strengthening and generalization of intrinsic ductile-to-brittle criterion, *Scientific Reports* 2 (1) (2012) 718.
  - [26] O. Senkov, D. Miracle, Generalization of intrinsic ductile-to-brittle criteria by Pugh and Pettifor for materials with a cubic crystal structure, *Scientific Reports* 11 (1) (2021) 4531.
  - [27] F. G. Coury, M. Kaufman, A. J. Clarke, Solid-solution strengthening in refractory high entropy alloys, *Acta Materialia* 175 (2019) 66–81.
  - [28] W. Lai, F. Vogel, X. Zhao, B. Wang, Y. Yi, D. You, X. Tong, W. Li, X. Yu, X. Wang, Design of bcc refractory multi-principal element alloys with superior mechanical properties, *Materials Research Letters* 10 (3) (2022) 133–140.
  - [29] W. Zheng, S. Lü, S. Wu, X. Chen, W. Guo, Development of  $\text{MoNbVTa}_x$  refractory high entropy alloy with high strength at elevated temperature, *Materials Science and Engineering: A* 850 (2022) 143554.
  - [30] C.-C. Juan, K.-K. Tseng, W.-L. Hsu, M.-H. Tsai, C.-W. Tsai, C.-M. Lin, S.-K. Chen, S.-J. Lin, J.-W. Yeh, Solution strengthening of ductile refractory  $\text{HfMo}_x\text{NbTaTiZr}$  high-entropy alloys, *Materials Letters* 175 (2016) 284–287.
  - [31] S. Foiles, M. Baskes, M. S. Daw, Embedded-atom-method functions for the fcc metals Cu, Ag, Au, Ni, Pd, Pt, and their alloys, *Physical Review B* 33 (12) (1986) 7983.
  - [32] Y. Mishin, Machine-learning interatomic potentials for materials science, *Acta Materialia* 214 (2021) 116980.
  - [33] M. E. Eberhart, T. E. Jones, Cauchy pressure and the generalized bonding model for nonmagnetic bcc transition metals, *Physical Review B* 86 (13) (2012) 134106.
  - [34] T. Nieh, J. Wadsworth, Recent advances and developments in refractory alloys, *MRS Online Proceedings Library (OPL)* 322 (1993) 315.
  - [35] S. Bijjala, P. Kumar, S. R. Atlas, Composition-dependent formation energies and band structures for the first-principles design of refractory binary alloys, in preparation (2024).
  - [36] N. Philips, M. Carl, N. Cunningham, New opportunities in refractory alloys, *Metallurgical and Materials Transactions A* 51 (2020) 3299–3310.
  - [37] K. Tanaka, M. Koiwa, Single-crystal elastic constants of intermetallic compounds, *Intermetallics* 4 (1996) S29–S39.
  - [38] G. Davies, R. O’Connell, Transducer and bond phase shifts in ultrasonics, and their effects on measured pressure derivatives of elastic moduli, in: *High-Pressure Research*, Elsevier, 1977, pp. 533–562.
  - [39] M. Beg, S. Shapiro, Study of phonon dispersion relations in cuprous oxide by inelastic neutron scattering, *Physical Review B* 13 (4) (1976) 1728.
  - [40] S. Shang, Y. Wang, Z.-K. Liu, First-principles elastic constants of  $\alpha$ - and  $\theta$ - $\text{Al}_2\text{O}_3$ , *Applied Physics Letters* 90 (10) (2007).
  - [41] Y.-J. Hu, A. Sundar, S. Ogata, L. Qi, Screening of generalized stacking fault energies, surface energies and intrinsic ductile potency of refractory multicomponent alloys, *Acta Materialia* 210 (2021) 116800.
  - [42] P. P. Borges, R. O. Ritchie, M. Asta, Local lattice distortions and the structural instabilities in bcc Nb–Ta–Ti–Hf high-entropy alloys: An ab initio computational study, *Acta Materialia* 262 (2024) 119415.
  - [43] S. A. Giles, D. Sengupta, S. R. Broderick, K. Rajan, Machine-learning-based intelligent framework for discovering refractory high-entropy alloys with improved high-temperature yield strength, *npj Computational Materials* 8 (1) (2022) 235.
  - [44] B. Vela, C. Acemi, P. Singh, T. Kirk, W. Trehern, E. Norris, D. D. Johnson, I. Karaman, R. Arróyave, High-throughput exploration of the  $\text{WMoVTaNbAl}$  refractory multi-principal-

- element alloys under multiple-property constraints, *Acta Materialia* 248 (2023) 118784.
- [45] P. Hohenberg, W. Kohn, Inhomogeneous electron gas, *Physical Review* 136 (3B) (1964) B864.
- [46] W. Kohn, L. Sham, Self-consistent equations including exchange and correlation effects, *Physical Review* 140 (4A) (1965) A1133.
- [47] A. H. Romero, D. C. Allan, B. Amadon, G. Antonius, T. Appencourt, L. Baguet, J. Bieder, F. Bottin, J. Bouchet, E. Bousquet, et al., Abinit: Overview and focus on selected capabilities, *The Journal of Chemical Physics* 152 (12) (2020).
- [48] A. Jain, S. P. Ong, G. Hautier, W. Chen, W. D. Richards, S. Dacek, S. Cholia, D. Gunter, D. Skinner, G. Ceder, et al., Commentary: The Materials Project: A materials genome approach to accelerating materials innovation, *APL Materials* 1 (1) (2013).
- [49] S. Curtarolo, W. Setyawan, G. L. Hart, M. Jahnatek, R. V. Chepulskii, R. H. Taylor, S. Wang, J. Xue, K. Yang, O. Levy, et al., Aflo: An automatic framework for high-throughput materials discovery, *Computational Materials Science* 58 (2012) 218–226.
- [50] A. Dal Corso, Elastic constants of beryllium: a first-principles investigation, *Journal of Physics: Condensed Matter* 28 (7) (2016) 075401.
- [51] F. Luo, L.-C. Cai, X.-R. Chen, F.-Q. Jing, D. Alfe, Ab initio calculation of lattice dynamics and thermodynamic properties of beryllium, *Journal of Applied Physics* 111 (5) (2012).
- [52] T. Shao, B. Wen, R. Melnik, S. Yao, Y. Kawazoe, Y. Tian, Temperature dependent elastic constants for crystals with arbitrary symmetry: Combined first principles and continuum elasticity theory, *Journal of Applied Physics* 111 (8) (2012).
- [53] G. Steinle-Neumann, L. Stixrude, R. E. Cohen, First-principles elastic constants for the hcp transition metals Fe, Co, and Re at high pressure, *Physical Review B* 60 (2) (1999) 791.
- [54] G. Simmons, Single crystal elastic constants and calculated aggregate properties, *A handbook* 4 (1971).
- [55] M. De Jong, W. Chen, T. Angsten, A. Jain, R. Notestine, A. Gamst, M. Sluiter, C. Krishna Ande, S. Van Der Zwaag, J. J. Plata, et al., Charting the complete elastic properties of inorganic crystalline compounds, *Scientific Data* 2 (1) (2015) 1–13.
- [56] O. Nielsen, R. M. Martin, First-principles calculation of stress, *Physical Review Letters* 50 (9) (1983) 697.
- [57] Y. Le Page, P. Saxe, Symmetry-general least-squares extraction of elastic data for strained materials from ab initio calculations of stress, *Physical Review B* 65 (10) (2002) 104104.
- [58] D. Jiang, Q. Zhou, L. Xue, T. Wang, J. Hu, First-principles study the phase stability and mechanical properties of binary W-Mo alloys, *Fusion Engineering and Design* 130 (2018) 56–61.
- [59] H. Li, C. Draxl, S. Wurster, R. Pippan, L. Romaner, Impact of *d*-band filling on the dislocation properties of bcc transition metals: The case of tantalum-tungsten alloys investigated by density-functional theory, *Physical Review B* 95 (9) (2017) 094114.
- [60] U. Bhandari, C. Zhang, S. Guo, S. Yang, First-principles study on the mechanical and thermodynamic properties of MoNbTaTiW, *International Journal of Minerals, Metallurgy and Materials* 27 (2020) 1398–1404.
- [61] P. Keuter, D. Music, M. Stuer, J. M. Schneider, Electronic structure tuning of the anomalous thermoelastic behavior in Nb-X (X= Zr, V, Mo) solid solutions, *Journal of Applied Physics* 125 (21) (2019).
- [62] S. Baroni, P. Giannozzi, A. Testa, Elastic constants of crystals from linear-response theory, *Physical Review Letters* 59 (23) (1987) 2662.
- [63] D. Hamann, X. Wu, K. M. Rabe, D. Vanderbilt, Metric tensor formulation of strain in density-functional perturbation theory, *Physical Review B* 71 (3) (2005) 035117.
- [64] D. Hamann, K. M. Rabe, D. Vanderbilt, Generalized-gradient-functional treatment of strain in density-functional perturbation theory, *Physical Review B* 72 (3) (2005) 033102.
- [65] W. Xifan, D. Vanderbilt, D. Hamann, Systematic treatment of displacements, strains, and electric fields in density-functional perturbation theory, *Physical Review B* 72 (3) (2005) 035105.
- [66] S. Baroni, S. De Gironcoli, A. Dal Corso, P. Giannozzi, Phonons and related crystal properties from density-functional perturbation theory, *Reviews of Modern Physics* 73 (2) (2001) 515.
- [67] X. Gonze, C. Lee, Dynamical matrices, Born effective charges, dielectric permittivity tensors, and interatomic force constants from density-functional perturbation theory, *Physical Review B* 55 (16) (1997) 10355–10368.
- [68] A. Martin, M. Torrent, R. Caracas, Projector augmented-wave formulation of response to strain and electric-field perturbation within density functional perturbation theory, *Physical Review B* 99 (9) (2019) 094112.
- [69] M.-M. Soumelidou, I. Belabbas, J. Kioseoglou, P. Komninou, J. Chen, T. Karakostas, Strain and elastic constants of GaN and InN, *Computational Condensed Matter* 10 (2017) 25–30.
- [70] G. Stenuit, S. Fahy, First-principles calculations of the mechanical and structural properties of GaN<sub>x</sub>As<sub>1-x</sub>: Lattice and elastic constants, *Physical Review B* 76 (3) (2007) 035201.
- [71] K. Bouamama, P. Djemia, N. Lebga, K. Kassali, Ab initio calculation of the elastic properties and the lattice dynamics of the Zn<sub>x</sub>Cd<sub>1-x</sub>Se alloy, *Semiconductor Science and Technology* 24 (4) (2009) 045005.
- [72] P. Daoust, M. Côté, P. Desjardins, R. A. Masut, Impact of applied biaxial stress on the piezoelectric, elastic, and dielectric properties of scandium aluminum nitride alloys determined by density functional perturbation theory, *AIP Advances* 11 (9) (2021).
- [73] P. Daoust, P. Desjardins, R. A. Masut, M. Côté, Longitudinal piezoelectric, elastic, and dielectric properties of rare-earth aluminum nitride alloys determined by density-functional perturbation theory, *Physical Review Materials* 6 (3) (2022) 034405.
- [74] T. Zhang, Y. Zheng, J. Chen, L. Song, E. Shi, First-principles study of microscopic origin of piezoelectric effect in  $\alpha$ -quartz, *Japanese Journal of Applied Physics* 45 (11R) (2006) 8755.
- [75] A. Zunger, S.-H. Wei, L. Ferreira, J. E. Bernard, Special quasirandom structures, *Physical Review Letters* 65 (3) (1990) 353.
- [76] X. Gonze, B. Amadon, G. Antonius, F. Arnardi, L. Baguet, J.-M. Beuken, J. Bieder, F. Bottin, J. Bouchet, E. Bousquet, et al., The Abinit project: Impact, environment and recent developments, *Computer Physics Communications* 248 (2020) 107042.
- [77] J. P. Perdew, K. Burke, M. Ernzerhof, Generalized gradient approximation made simple, *Physical Review Letters* 77 (18) (1996) 3865.
- [78] M. J. Van Setten, M. Giantomassi, E. Bousquet, M. J. Verstraete, D. R. Hamann, X. Gonze, G.-M. Rignanese, The pseudodojo: Training and grading a 85 element optimized norm-conserving pseudopotential table, *Computer Physics Communications* 226 (2018) 39–54.
- [79] J. W. Furness, A. D. Kaplan, J. Ning, J. P. Perdew, J. Sun, Accurate and numerically efficient r2SCAN meta-generalized gradient approximation, *The Journal of Physical Chemistry Letters* 11 (19) (2020) 8208–8215.
- [80] V. I. Anisimov, J. Zaanen, O. K. Andersen, Band theory and Mott insulators: Hubbard *U* instead of Stoner *I*, *Physical Re-*

- view B 44 (3) (1991) 943.
- [81] R. Kingsbury, A. S. Gupta, C. J. Bartel, J. M. Munro, S. Dwaraknath, M. Horton, K. A. Persson, Performance comparison of r2SCAN and SCAN metaGGA density functionals for solid materials via an automated, high-throughput computational workflow, *Physical Review Materials* 6 (1) (2022) 013801.
- [82] H. J. Monkhorst, J. D. Pack, Special points for Brillouin-zone integrations, *Physical Review B* 13 (12) (1976) 5188.
- [83] Abinit, [https://abinit.github.io/abinit\\_web/pseudopotential.html](https://abinit.github.io/abinit_web/pseudopotential.html) (2024).
- [84] Pseudo-dojo, <https://www.pseudo-dojo.org> (2024).
- [85] P. E. Blöchl, Projector augmented-wave method, *Physical Review B* 50 (24) (1994) 17953.
- [86] A. Van De Walle, M. Asta, G. Ceder, The alloy theoretic automated toolkit: A user guide, *Calphad* 26 (4) (2002) 539–553.
- [87] C. Jiang, C. Wolverton, J. Sofo, L.-Q. Chen, Z.-K. Liu, First-principles study of binary bcc alloys using special quasirandom structures, *Physical Review B* 69 (21) (2004) 214202.
- [88] M. Verstraete, X. Gonze, Smearing scheme for finite-temperature electronic-structure calculations, *Physical Review B* 65 (3) (2001) 035111.
- [89] X. Gonze, First-principles responses of solids to atomic displacements and homogeneous electric fields: Implementation of a conjugate-gradient algorithm, *Physical Review B* 55 (1997) 10337–10354.
- [90] J. Zhao, J. Winey, Y. Gupta, First-principles calculations of second- and third-order elastic constants for single crystals of arbitrary symmetry, *Physical Review B* 75 (9) (2007) 094105.
- [91] O. Redlich, A. Kister, Algebraic representation of thermodynamic properties and the classification of solutions, *Industrial & Engineering Chemistry* 40 (2) (1948) 345–348.
- [92] A. Korenev, A. Illarionov, The calculated and experimental elastic properties of quenched biocompatible Ti–Nb, Ti–Nb–Zr, Ti–Nb–Zr–Sn, and Ti–Nb–Zr–Sn–Ta titanium alloys, *Physics of Metals and Metallography* 123 (11) (2022) 1132–1138.
- [93] Z. Liu, H. Zhang, S. Ganeshan, Y. Wang, S. Mathaudhu, Computational modeling of effects of alloying elements on elastic coefficients, *Scripta Materialia* 63 (7) (2010) 686–691.
- [94] J. F. Nye, *Physical Properties of Crystals: Their Representation by Tensors and Matrices*, Oxford University Press, New York, 1985.
- [95] D. Tromans, Elastic anisotropy of HCP metal crystals and polycrystals, *Int. J. Res. Rev. Appl. Sci* 6 (4) (2011) 462–483.
- [96] C. Kittel, P. McEuen, *Introduction to Solid State Physics*, John Wiley & Sons, 2018.
- [97] A. R. Denton, N. W. Ashcroft, Vegard’s law, *Physical Review A* 43 (6) (1991) 3161.
- [98] W. Hubbell, F. Brotzen, Elastic constants of niobium-molybdenum alloys in the temperature range  $-190$  to  $+100^\circ\text{C}$ , *Journal of Applied Physics* 43 (8) (1972) 3306–3312.
- [99] D. Armstrong, B. Mordike, The influence of alloying and temperature on the elastic constants of tantalum, *Journal of the Less Common Metals* 22 (3) (1970) 265–274.
- [100] M. Frey, J. Lonnee, G. Shannette, Elastic constants of niobium-zirconium, hafnium, and tungsten alloys, *Journal of Applied Physics* 49 (8) (1978) 4406–4410.
- [101] B. Auld, R. E. Green, *Acoustic Fields and Waves in Solids*, Wiley, New York, 1973.
- [102] W. Knabl, G. Leichtfried, R. Stickler, Refractory metals and refractory metal alloys, *Springer Handbook of Materials Data* (2018) 307–337.
- [103] D. G. Pettifor, M. Aoki, Bonding and structure of intermetallics: a new bond order potential, *Philosophical Transactions of the Royal Society of London. Series A: Physical and Engineering Sciences* 334 (1635) (1991) 439–449.
- [104] J. J. Gilman, *Electronic basis of the strength of materials*, Cambridge University Press, 2003.
- [105] R. Thompson, W. Clegg, Predicting whether a material is ductile or brittle, *Current Opinion in Solid State and Materials Science* 22 (3) (2018) 100–108.
- [106] R. Gaillac, P. Pullumbi, F.-X. Coudert, Elate: an open-source online application for analysis and visualization of elastic tensors, *Journal of Physics: Condensed Matter* 28 (27) (2016) 275201.
- [107] Y. Ye, Y. Zhang, Q. He, Y. Zhuang, S. Wang, S. Shi, A. Hu, J. Fan, Y. Yang, Atomic-scale distorted lattice in chemically disordered equimolar complex alloys, *Acta Materialia* 150 (2018) 182–194.
- [108] P. Pyykkö, M. Atsumi, Molecular single-bond covalent radii for elements 1–118, *Chemistry—A European Journal* 15 (1) (2009) 186–197.
- [109] X. Wu, D. Vanderbilt, D. Hamann, Systematic treatment of displacements, strains, and electric fields in density-functional perturbation theory, *Physical Review B* 72 (3) (2005) 035105.
- [110] Y. Zhang, T. T. Zuo, Z. Tang, M. C. Gao, K. A. Dahmen, P. K. Liaw, Z. P. Lu, Microstructures and properties of high-entropy alloys, *Progress in Materials Science* 61 (2014) 1–93.
- [111] L. R. Owen, N. G. Jones, Lattice distortions in high-entropy alloys, *Journal of Materials Research* 33 (19) (2018) 2954–2969.
- [112] R. L. Fleischer, Substitutional solution hardening, *Acta Metallurgica* 11 (3) (1963) 203–209.
- [113] R. Labusch, A statistical theory of solid solution hardening, *physica status solidi (b)* 41 (2) (1970) 659–669.
- [114] Q. He, Y. Yang, On lattice distortion in high entropy alloys, *Frontiers in Materials* 5 (2018) 42.
- [115] I. Toda-Caraballo, P. E. Rivera-Díaz-del Castillo, Modelling solid solution hardening in high entropy alloys, *Acta Materialia* 85 (2015) 14–23.
- [116] L.-Y. Tian, Q.-M. Hu, R. Yang, J. Zhao, B. Johansson, L. Vitos, Elastic constants of random solid solutions by SQS and CPA approaches: the case of fcc Ti–Al, *Journal of Physics: Condensed Matter* 27 (31) (2015) 315702.
- [117] E. K. Delczeg-Czirjak, L. Delczeg, M. Ropo, K. Kokko, M. Punkkinen, B. Johansson, L. Vitos, Ab initio study of the elastic anomalies in Pd–Ag alloys, *Physical Review B* 79 (8) (2009) 085107.
- [118] D. B. Miracle, O. N. Senkov, A critical review of high entropy alloys and related concepts, *Acta Materialia* 122 (2017) 448–511.

## 6. Appendix

The following figures provide additional computational results for binaries not discussed in the main text. Figures 9–12 illustrate the spatial dependence of  $G$  (GPa),  $E$  (GPa), and  $\nu$  for MoTa, MoW, NbTa and WNb, as a function of composition. Figures 13–16 illustrate the relaxation field of  $\bar{C}_{11}$ ,  $\bar{C}_{12}$ ,  $\bar{C}_{44}$  and  $G$  as a function of composition for MoNb, MoTa, MoW and WNb.

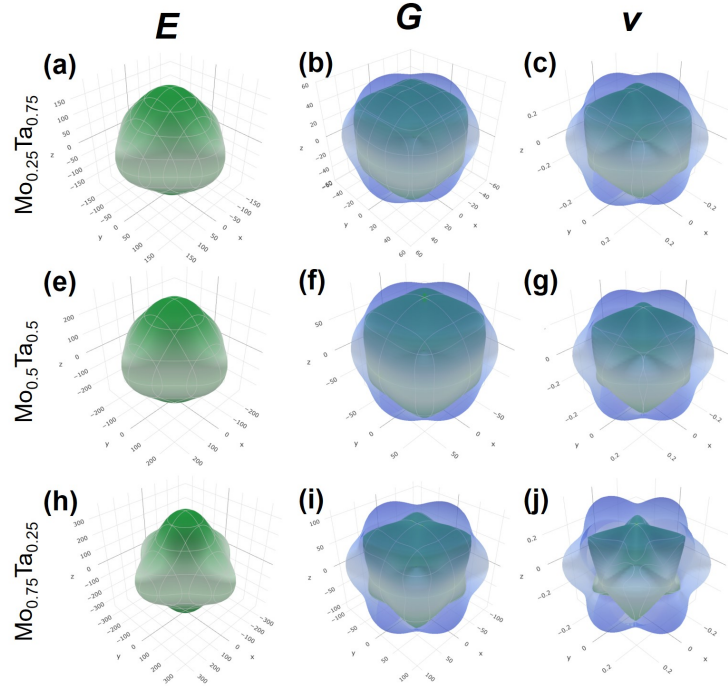


Figure 9: Spatial dependence of  $G$  (GPa),  $E$  (GPa), and  $\nu$  for: (a)-(c)  $\text{Mo}_{0.25}\text{Ta}_{0.75}$ ; (d)-(f)  $\text{Mo}_{0.5}\text{Ta}_{0.5}$ ; and (g)-(h)  $\text{Mo}_{0.75}\text{Ta}_{0.25}$ . Plots generated using the ELATE tool [106]. The maximum and minimum values of  $G$ ,  $E$  and  $\nu$  are represented as transparent blue and solid green surfaces respectively.

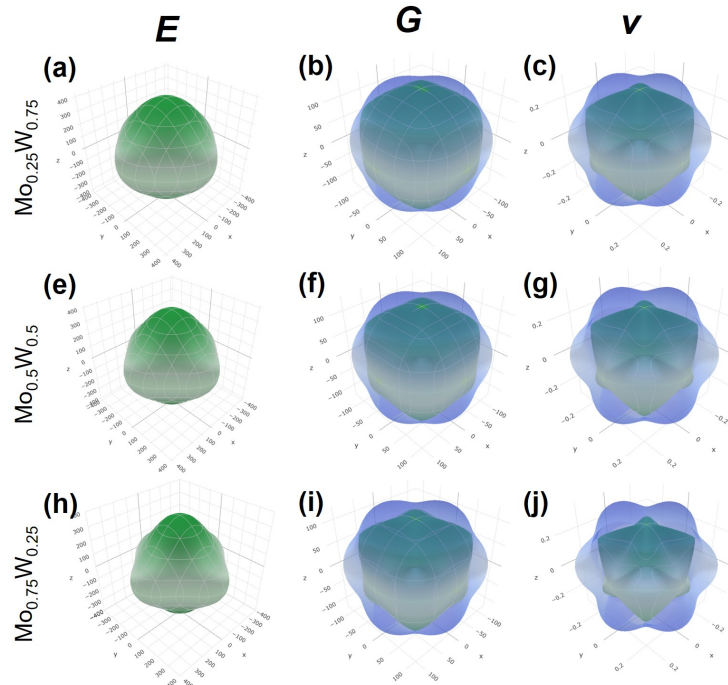


Figure 10: Spatial dependence of  $G$  (GPa),  $E$  (GPa) and  $\nu$  for: (a)-(c)  $\text{Mo}_{0.25}\text{W}_{0.75}$ ; (d)-(f)  $\text{Mo}_{0.5}\text{W}_{0.5}$ ; and (g)-(h)  $\text{Mo}_{0.75}\text{W}_{0.25}$ . Plots generated using the ELATE tool [106]. The maximum and minimum values of  $G$ ,  $E$  and  $\nu$  are represented as transparent blue and solid green surfaces respectively.

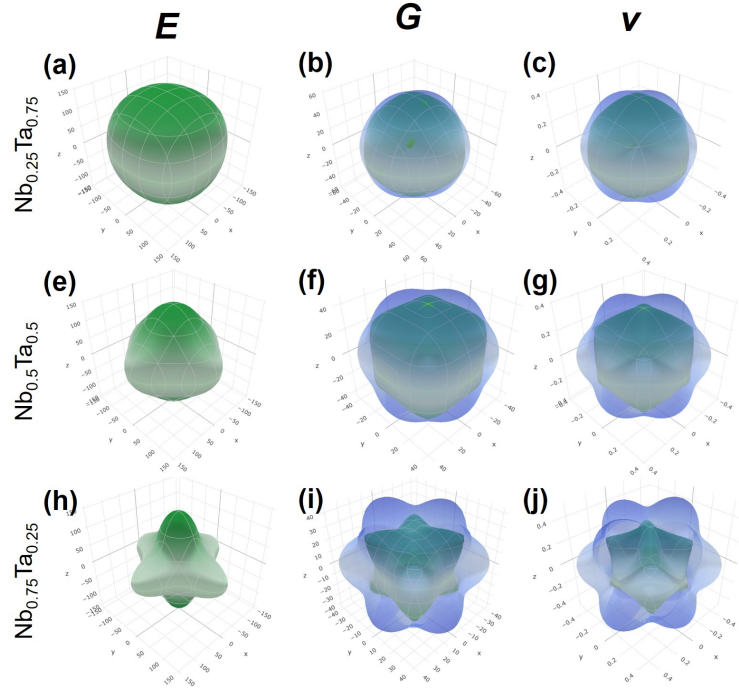


Figure 11: Spatial dependence of  $G$  (GPa),  $E$  (GPa) and  $\nu$  for: (a)-(c)  $\text{Nb}_{0.25}\text{Ta}_{0.75}$ ; (d)-(f)  $\text{Nb}_{0.5}\text{Ta}_{0.5}$ ; and (g)-(h)  $\text{Nb}_{0.75}\text{Ta}_{0.25}$ . Plots generated using the ELATE tool [106]. The maximum and minimum values of  $G$ ,  $E$  and  $\nu$  are represented as transparent blue and solid green surfaces respectively.

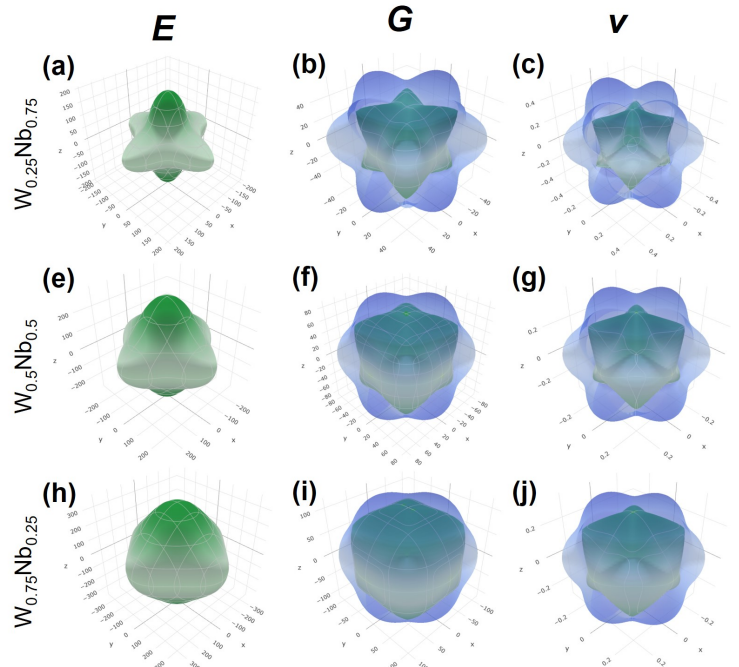


Figure 12: Spatial dependence of  $G$  (GPa),  $E$  (GPa) and  $\nu$  for: (a)-(c)  $\text{W}_{0.25}\text{Nb}_{0.75}$ ; (d)-(f)  $\text{W}_{0.5}\text{Nb}_{0.5}$ ; and (g)-(h)  $\text{W}_{0.75}\text{Nb}_{0.25}$ . Plots generated using the ELATE tool [106]. The maximum and minimum values of  $G$ ,  $E$  and  $\nu$  are represented as transparent blue and solid green surfaces respectively.

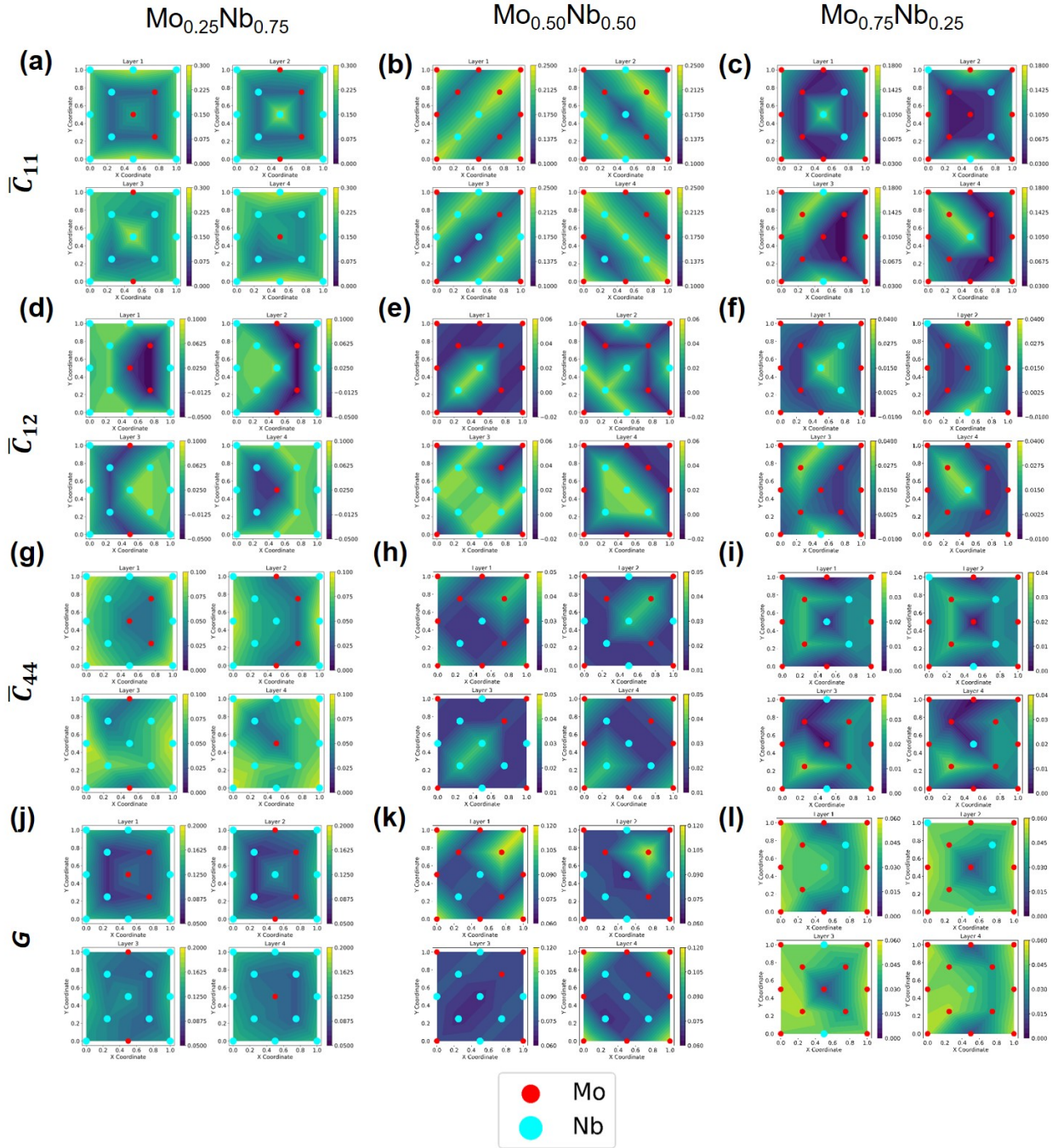


Figure 13: Relaxation field (values in GPa) constructed as described in text for  $\text{Mo}_{0.25}\text{Nb}_{0.75}$ ,  $\text{Mo}_{0.5}\text{Nb}_{0.5}$ , and  $\text{Mo}_{0.75}\text{Nb}_{0.25}$ . (a)-(c):  $\bar{C}_{11}$ , (d)-(f):  $\bar{C}_{12}$ , (g)-(i):  $\bar{C}_{44}$ , and (j)-(l):  $G$ . The color bar is set to range from minimum to maximum relaxation values for all atoms.  $x$  and  $y$  coordinates correspond to reduced coordinates in the 3D supercell.

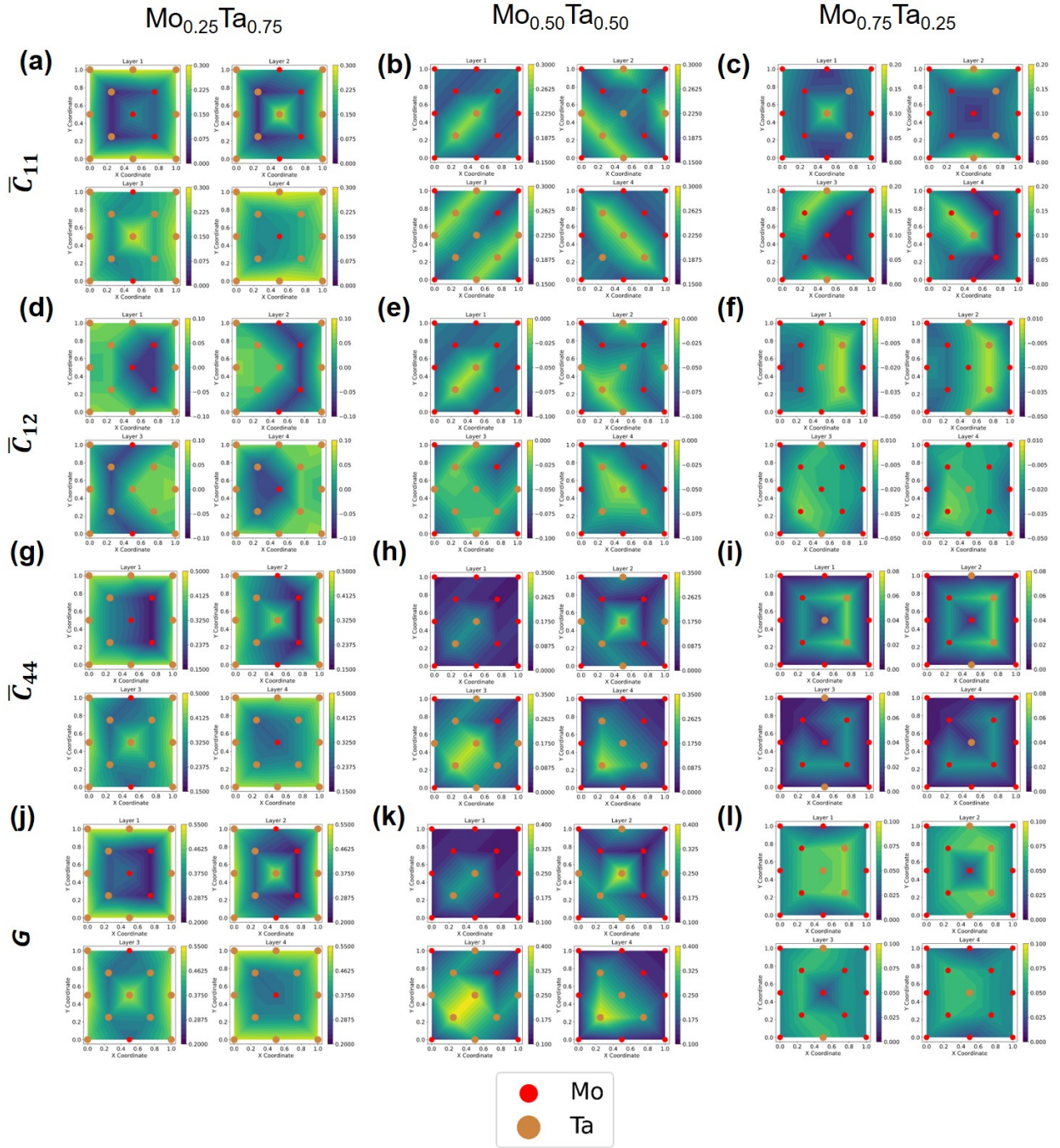


Figure 14: Relaxation field (values in GPa) constructed as described in text for  $\text{Mo}_{0.25}\text{Ta}_{0.75}$ ,  $\text{Mo}_{0.5}\text{Ta}_{0.5}$ , and  $\text{Mo}_{0.75}\text{Ta}_{0.25}$ . (a)-(c):  $\bar{C}_{11}$ , (d)-(f):  $\bar{C}_{12}$ , (g)-(i):  $\bar{C}_{44}$ , and (j)-(l):  $G$ . The color bar is set to range from minimum to maximum relaxation values for all atoms.  $x$  and  $y$  coordinates correspond to reduced coordinates in the 3D supercell.



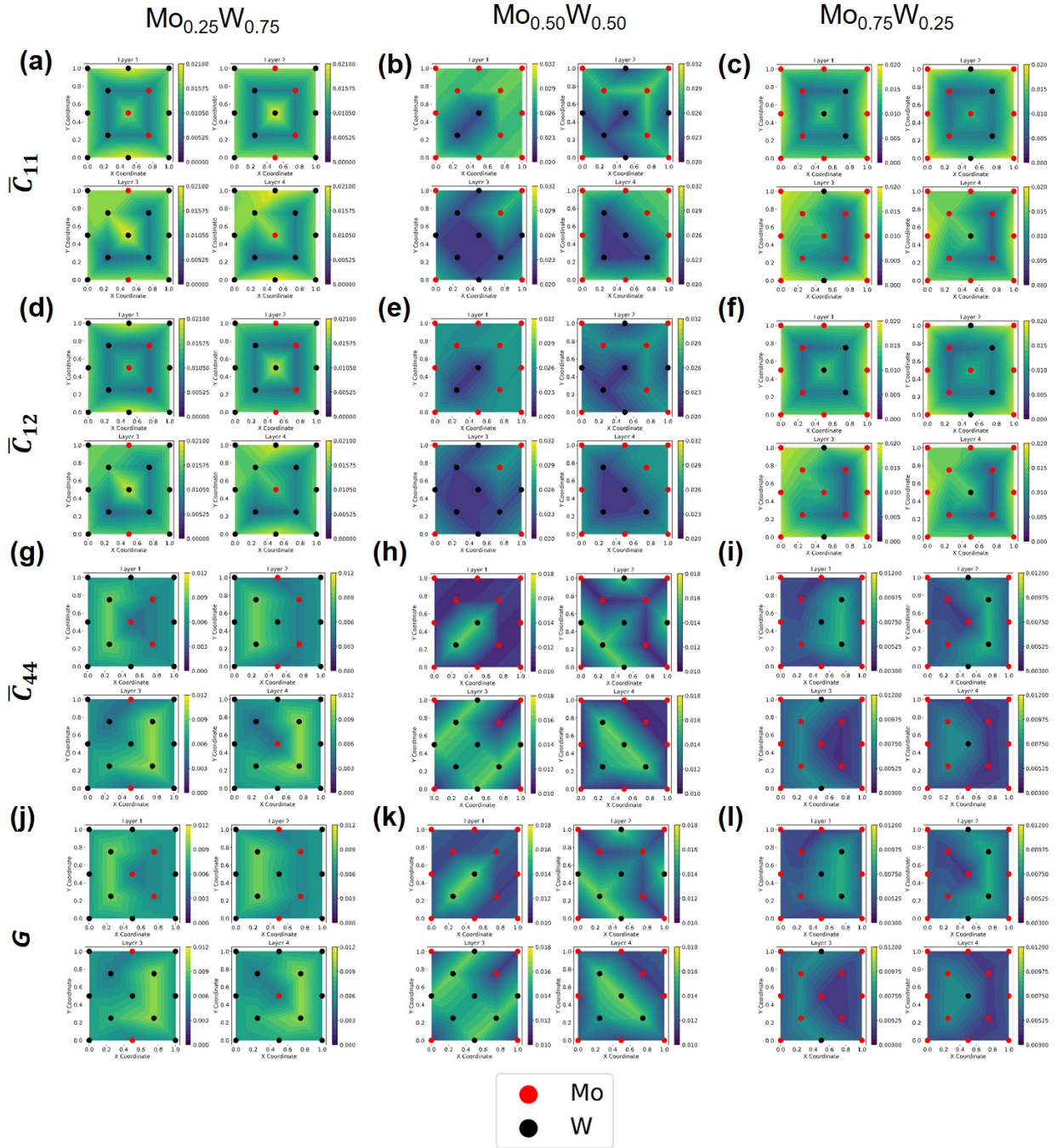


Figure 15: Relaxation field (values in GPa) constructed as described in text for  $Mo_{0.25}W_{0.75}$ ,  $Mo_{0.5}W_{0.5}$ , and  $Mo_{0.75}W_{0.25}$ . (a)-(c):  $\bar{C}_{11}$ , (d)-(f):  $\bar{C}_{12}$ , (g)-(i):  $\bar{C}_{44}$ , and (j)-(l):  $G$ . The color bar is set to range from minimum to maximum relaxation values for all atoms.  $x$  and  $y$  coordinates correspond to reduced coordinates in the 3D supercell.

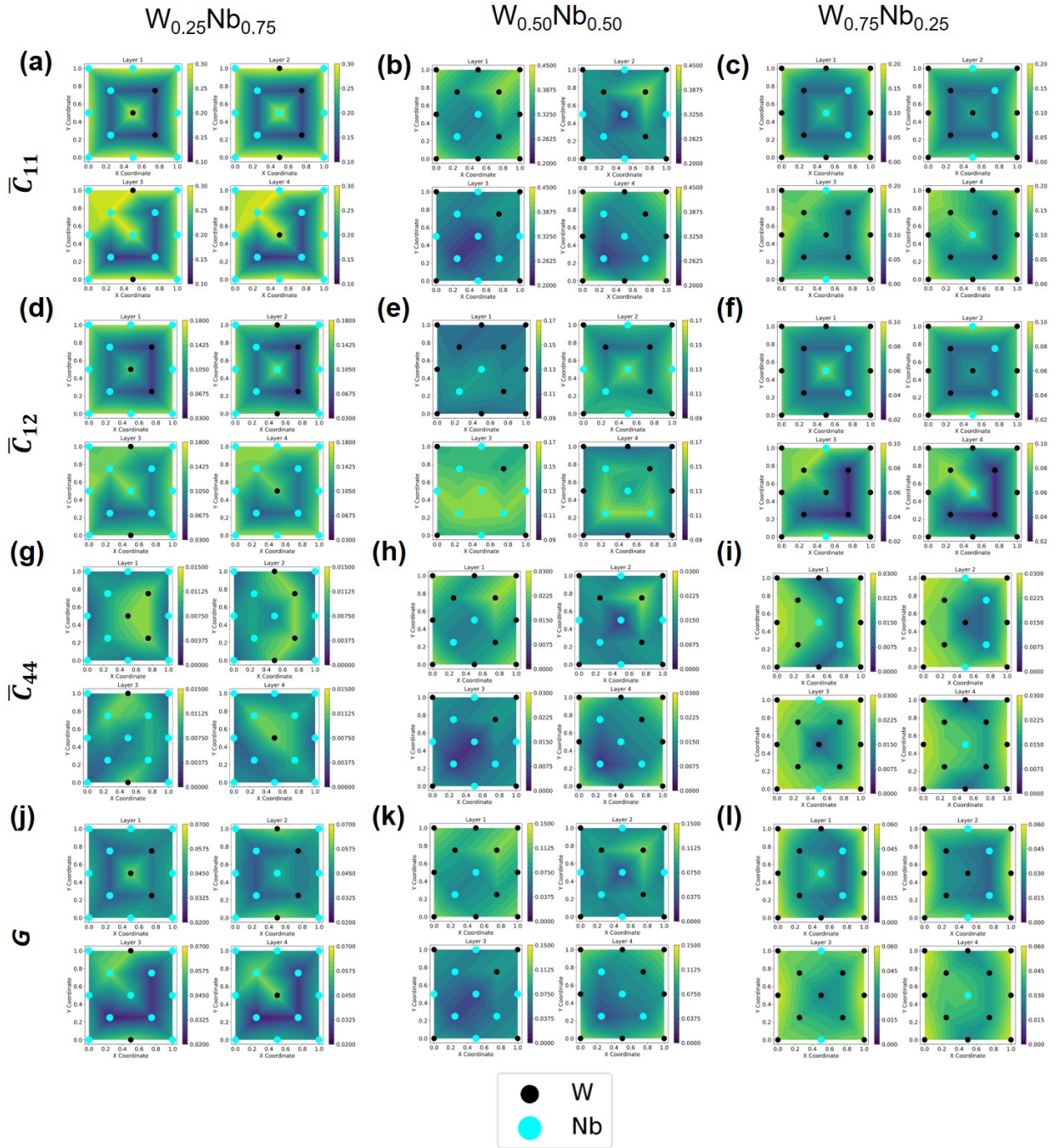


Figure 16: Relaxation field (values in GPa) constructed as described in text for  $W_{0.25}Nb_{0.75}$ ,  $W_{0.5}Nb_{0.5}$ , and  $W_{0.75}Nb_{0.25}$ . (a)-(c):  $\bar{C}_{11}$ , (d)-(f):  $\bar{C}_{12}$ , (g)-(i):  $\bar{C}_{44}$ , and (j)-(l):  $G$ . The color bar is set to range from minimum to maximum relaxation values for all atoms.  $x$  and  $y$  coordinates correspond to reduced coordinates in the 3D supercell.